Electrification of Stratiform Regions in Mesoscale Convective Systems. Part I: An Observational Comparison of Symmetric and Asymmetric MCSs

TERRY J. SCHUUR* AND STEVEN A. RUTLEDGE

Department of Atmospheric Science, Colorado State University, Fort Collins, Colorado

(Manuscript received 14 December 1998, in final form 30 July 1999)

ABSTRACT

The kinematic, microphysical, and electrical structures of two mesoscale convective systems (MCSs) observed during the 1991 Cooperative Oklahoma Profiler Studies (COPS91) experiment are analyzed. Profiles of the vertical electric field structure and charge density were obtained from a series of balloon-borne electric field meter (EFM) flights into each MCS. Contrasting electric field structures were found in the stratiform regions of these MCSs. In both systems, the EFM data indicate that the MCS charge structure was characterized by horizontally extensive regions of charge and charge density magnitudes on the order of what is typically observed in convective cores ($\leq$5 nC m^{-3}). However, the vertical electric field profiles were each related to unique MCS precipitation and kinematic structures, with a five-layer charge profile (at $T \leq 0$°C) associated with the ''symmetric'' MCS and a simpler three-layer charge profile (at $T \leq 0$°C) associated with the ''asymmetric'' MCSs.

The observational analysis identified several kinematic, thermodynamic, and microphysical differences between the two systems that offer at least some explanation for the observed electrical structures. First, ice particles detrained from the convective line of the symmetric MCS had much shorter ''residence times'' in the unfavorable growth/charging region associated with the transition zone downdraft compared to the asymmetric case. Second, upon entering the trailing stratiform region, ice particles in the symmetric system were immersed in an environment that was more conducive to in situ charging via noninductive charging mechanisms. Strong mesoscale ascent in the stratiform region of the symmetric MCS led to the presence of supercooled cloud water, and hence significant electrification. There are also indications that fallspeed differences between particle types may be responsible for producing some of the charge transitions in the electric field profiles. In contrast, strong mesoscale ascent was not present in the asymmetric case, and hence conditions were less favorable for noninductive charging.

1. Introduction

Over the past decade, much has been learned regarding the precipitation patterns and kinematic structures of midlatitude mesoscale convective systems (MCSs). In particular, studies have shown that their precipitation structures can often be classified into distinct categories (e.g., Houze et al. 1989; Blanchard 1990; Houze et al. 1990) with two of the more common types of organization being 1) a quasi-linear convective line trailed along its entire length by stratiform precipitation (symmetric MCS), and 2) a bowed convective line with a region of stratiform precipitation associated with the northern portion of the convective line (asymmetric MCS). Conceptual models depicting the precipitation and kinematic structures of these two MCS types are shown in Fig. 1. Symmetric MCSs often evolve into asymmetric MCSs during their later stages (e.g., Rutledge et al. 1988; Houze et al. 1989; Loehrer and Johnson 1995).

Observational studies of MCS microphysical structures are less common. According to Houze (1989), ice generated in convective line updrafts is advected rearward in the mesoscale front-to-rear airflow where it bridges a weak reflectivity region, commonly known as a transition zone (e.g., Smull and Houze 1985), and is distributed into the mesoscale updraft. A conceptual model depicting the microphysical structure of a symmetric MCS (oriented along a line analogous to AB in Fig. 1) is shown in Fig. 2. Once in the mesoscale updraft, ice particles continue to grow by vapor deposition in a seeder–feeder-type process (e.g., Rutledge and Houze 1987). The evolution of hydrometeors as they pass through the weaker reflectivity, transition zone region is less well known. It is widely accepted that deep subsidence in some regions of the transition zone results in either sublimation (e.g., Smull and Houze 1985) or

* Current affiliation: NOAA/ERL/National Severe Storms Laboratory, and Cooperative Institute for Mesoscale Meteorological Studies, Norman, Oklahoma.

Corresponding author address: Dr. Terry J. Schuur, National Severe Storms Laboratory, 1313 Halley Circle, Norman, OK 73069.
E-mail: Terry.Schuur@nssl.noaa.gov

© 2000 American Meteorological Society

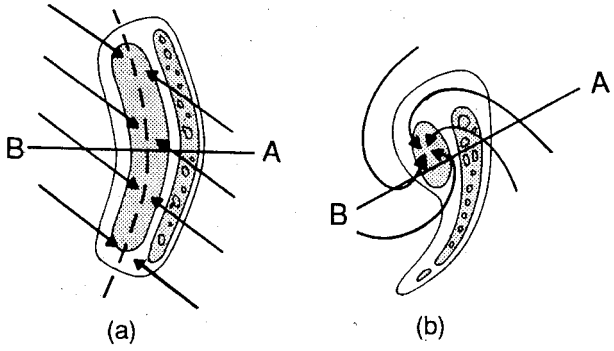

FIG. 1. Conceptual model of midlevel horizontal cross section through (a) a symmetric MCS and (b) an asymmetric MCS. In each case, the midlevel, system-relative airflow is overlaid on the low-level radar reflectivity pattern. Shading indicates regions of higher reflectivity. Line AB indicates location of vertical cross section depicted by Houze et al. (1989). (From Houze et al. 1989.)

suppressed growth (e.g., Biggerstaff and Houze 1993; Braun and Houze 1994) of hydrometeors. In addition to depositional growth, ice particles in the stratiform region grow by aggregation (Houze and Churchill 1984; Yeh et al. 1991). Growth by riming can also occur (Leary and Houze 1979; Rutledge and Houze 1987).

Previous studies of MCS electrification focused on the frequent production of positive cloud-to-ground lightning flashes in the stratiform region (e.g., Orville et al. 1988; Rutledge and MacGorman 1988; Rutledge et al. 1990; Engholm et al. 1990; Rutledge and Petersen 1994; MacGorman and Rust 1998). More recently, balloon-borne electric field meter (EFM) observations (e.g., Schuur et al. 1991; Hunter et al. 1992; Marshall and Rust 1993; Stolzenburg et al. 1994) have consistently shown that electric fields and charge densities are the same order of magnitude as those observed in convective cores (i.e., >100 kV m^{-1} and >3 nC m^{-3}, respectively). In particular, and most relevant to this study, Marshall and Rust (1993) noted that the symmetric and asymmetric MCS structures appear to exhibit distinctly different electrical structures. Symmetric MCSs (Fig. 1a) exhibited a complicated five-layer charge structure (for $T < 0$°C), while asymmetric MCSs (Fig. 1b) had a much simpler three-layer charge structure (for $T < 0$°C). They referred to these two electric field profiles as ''type A'' and ''type B,'' respectively, and remarked that MCS stratiform charge structure was much more repeatable than is commonly observed in individual convective cells. They also suggested these different electrical structures might be related to differences in the MCS's flow structures, microphysical structures, or both.

In this study we address the concurrent kinematic, microphysical, and electrical structures of one symmetric and one asymmetric MCS to identify potential kinematic and microphysical differences that might account for these unique and repeatable electric field structures. In particular, we focus on each MCS's mesoscale vertical motion pattern, microphysical structure, and charge transition levels (i.e., locations where charge polarity changes sign). We are especially interested in examining the ability of the mesoscale updrafts to produce water-saturated conditions necessary for significant noninductive charging. The results from these observational analyses are then presented as refined conceptual models for each MCS type (symmetric and asymmetric), as a result of comprehensive datasets collected in each of these cases. Finally, in a companion paper (Schuur and Rutledge 2000, hereafter Part II), we investigate the electrification of a symmetric MCS with a two-dimensional cloud model.

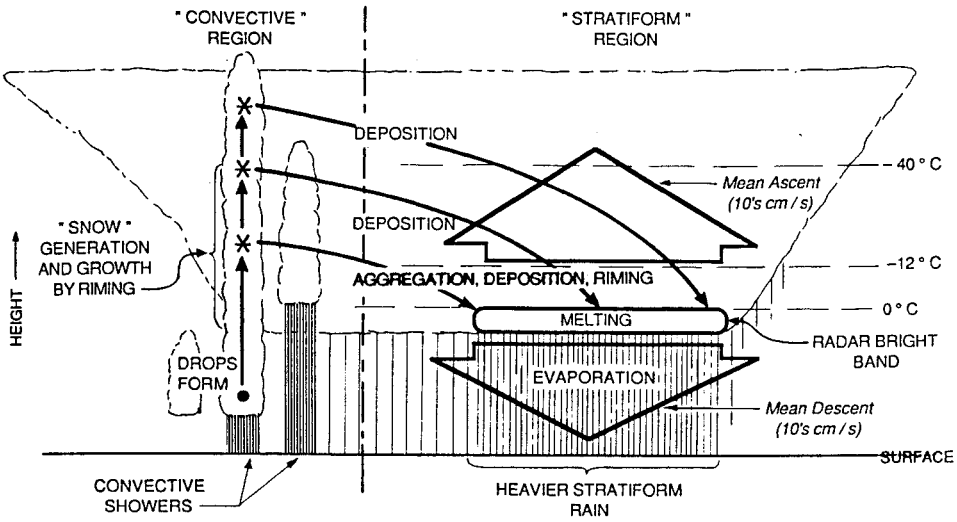

FIG. 2. Conceptual model of the microphysical structure of a symmetric MCS as viewed in a vertical cross section oriented normal to the convective line (along line AB in Fig. 1). (From Houze 1989.)

2. Instrumentation and data analysis

During the spring of 1991, the National Severe Storms Laboratory (NSSL), in collaboration with several university groups, conducted the Cooperative Oklahoma Profiler Studies (COPS91) project over central Oklahoma. One of the primary objectives of COPS91 was to investigate the charge structure and electrical development of midlatitude MCSs. Whereas earlier MCS electrification studies (e.g., Schuur et al. 1991; Hunter et al. 1992) typically relied upon single EFM profiles and limited supplemental data, the COPS91 experiment focused on the collection of multiple EFM datasets and simultaneous in situ National Oceanic and Atmospheric Administration (NOAA) P-3 aircraft measurements of MCS kinematic, microphysical, and thermodynamic structures. We focus on the study of the 24 May 1991 MCS (symmetric case) and 8 May 1991 MCS (asymmetric case) in this study. A discussion of the data sources and analysis methods used in this study is presented in the appendix.

3. Kinematic, microphysical, and electrical observations

We now present a brief description of the symmetric and asymmetric MCSs that are the subject of this study, focusing on each system's concomitant vertical motion, microphysical, and electrical structures. A more detailed discussion is presented by Schuur (1997).

a. Symmetric MCS

At 1200 UTC on 23 May 1991, a well-defined, north–south-oriented dryline extended across extreme eastern New Mexico. Ahead of the dryline, weak southeasterly surface winds were advecting moisture laden air from the Gulf of Mexico northwestward into central Oklahoma (where dewpoints reached 20°C). Behind the dryline, winds veered to a west-southwesterly direction while dewpoints dropped to approximately 2°C. A strong southerly jet was centered over west Texas at 850 mb, while at 500 mb a weak short-wave trough was approaching from the southwest. These two features combined to destabilize the atmosphere over the Texas Panhandle throughout the day as lifted indices over west Texas reached −10°C by midafternoon. By 1600 UTC, a small region of intense convection had broken out over northwestern Oklahoma and a north–south line of strong thunderstorms began to develop along the dryline over extreme eastern New Mexico. These two convective regions merged by 0400 UTC to form the quasi-linear, north–south-oriented convective line that is the subject of this study. Figures 3 and 4 depict the low-level radar reflectivity structure of the symmetric at 0545 and 0700 UTC, which are the approximate times (0549 and 0705 UTC, respectively) of the two symmetric MCS EFM flights.

1) KINEMATIC STRUCTURE

As the MCS moved through western Oklahoma, the P-3 conducted a series of 10 flight legs (representing ~930 km of aircraft track data) through the transition zone. Though some evolution occurred over this 3-h time period, a comparison of the dual-Doppler grids constructed from these flight legs reveals that the basic horizontal flow structure was rather steady in time. Overall, system-relative winds derived from these dual-Doppler analyses exhibited many similarities to those depicted for the symmetric MCS conceptual model (see Fig. 1a). At low levels, winds had a weak rear-to-front component, indicative of a rear-inflow jet. Above this, a transition in wind direction/speed resulted in a dominant front-to-rear airflow regime that also had a slight line-parallel component at heights above 3 km.

Using the 10 dual-Doppler grids, vertical velocities were derived using the compositing technique described in the appendix. Here we present reflectivity and vertical velocity composites for both a single flight leg (Fig. 5) and a space–time composite of all 10 flight legs (Fig. 6). As seen in Fig. 5, a 10-km-wide region of deep subsidence was located approximately 15–20 km behind the convective line. In agreement with the results of Biggerstaff and Houze (1993), this downdraft region appears to have consisted of two distinct parts: 1) an upper-level downdraft, which Biggerstaff and Houze proposed was mechanically forced by colliding convective outflows; and 2) a low-level downdraft, which Biggerstaff and Houze suggested was primarily the result of cooling processes (i.e., sublimation, evaporation, and melting). Behind this region of deep subsidence was a broad region of mesoscale ascent, which appeared to be most intense and deep at a location that preceded the leading edge of the stratiform precipitation region bright band by approximately 10 km. Peak vertical motions in this updraft region were >50 cm s^{-1}.

This same basic structure of mesoscale vertical motion, albeit with weaker mean vertical motions, is shown by the space–time composite in Fig. 6. Since this represents a spatial and temporal average, certain evolutionary features are lost in this analysis. For example, single-Doppler analyses of the MCS by the NSSL Cimarron radar (not shown) indicated a slight rearward tilting of the MCS convection with time in a manner similar to that described by the modeling studies of Rotunno et al. (1988) and Fovell and Ogura (1988), and in the observational study of Rasmussen and Rutledge (1993). A similar vertical motion structure was found when compositing was done with respect to the leading edge of the transition zone (see the appendix), though the space–time composite in that analysis better revealed the deep transition zone downdraft (e.g., Schuur 1997).

2) MICROPHYSICAL STRUCTURE

The P-3 conducted a spiral descent at the time and approximate location of the second EFM launch. Un-

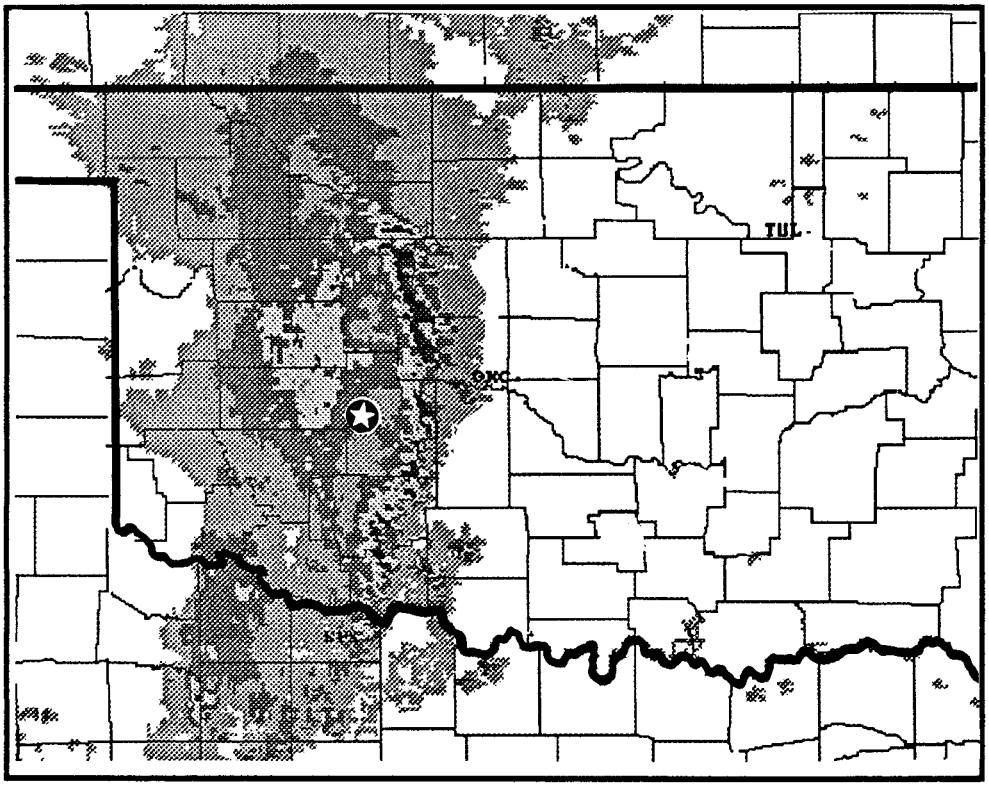

FIG. 3. Location of 0549 UTC 24 May 1991 electric field meter launch site (indicated by star) overlaid on composite of low-level radar reflectivity patterns of the 24 May 1991 (symmetric) MCS at 0545 UTC. Radar reflectivity ranges of 18–30, 30–41, 41–46, and >46 dB*Z*, respectively.

fortunately, due to tape drive problems, microphysical data were not recorded over much of the descent and only data for $T > -8$°C were available for analysis. The 2D-C and 2D-P shadow graph imagery collected at −8°C in the spiral descent are presented in Fig. 7. Probably the most striking feature in both the 2D-C and 2D-P shadow graph imagery is the presence of significant dendritic growth with sizes that ranged from <1 to >3 mm. Since it is well known that dendritic growth occurs under water-saturated conditions (e.g., Magono and Lee 1966; Ryan et al. 1976; Keller and Hallett 1982), these images suggest that water-saturated conditions, and therefore significant updrafts, were likely present above the −8°C level. The shadow graph imagery further indicates the presence of aggregates of dendrites. Liquid water contents (LWCs) observed during most flight legs ranged from 0.1 to 0.5 g m^{-3} with averages over most flight legs between 0.2 and 0.25 g m^{-3}. Localized pockets of enhanced LWCs as high as 0.5 g m^{-3} suggests the presence of embedded convective elements within the mesoscale updraft. In addition, data from the advecting spiral descent were averaged over the −16° to −8°C layer, which encompassed one of the primary charge transitions in the symmetric MCS electric field profiles. Mean cloud liquid water contents exceeded 0.2 g m^{-3} over this layer, consistent with the presence of dendritic crystals that require water-saturated conditions. Obviously riming would also occur under these conditions. Zrnic et al. (1993) also suggested the presence of supercooled cloud water in the stratiform region.

Two-dimensional shadow graph imagery from the transition zone flight legs consistently revealed a wide variety of particle habits, including lightly rimed columns, needles, and graupel with sizes as large as 2 mm. Small aggregates were occasionally observed, but were typically much smaller than the ice particles observed in the stratiform precipitation region. This is similar to the results of Yeh et al. (1991), who suggested that the lower reflectivity associated with the transition zone was likely the result of mean hydrometeor sizes that were approximately half of those found in the trailing stratiform precipitation region (even though the particle concentrations in the transition zone were much larger). Using software and artifact elimination procedures (see the appendix), short segments of data from selected flight legs were analyzed to reveal hydrometeor concentrations that were as high as 40 L^{-1} for the precipitation-sized particles and 300 L^{-1} for the cloud-sized particles at locations immediately behind the convective line at $T = -10$°C. These observations are used in Part

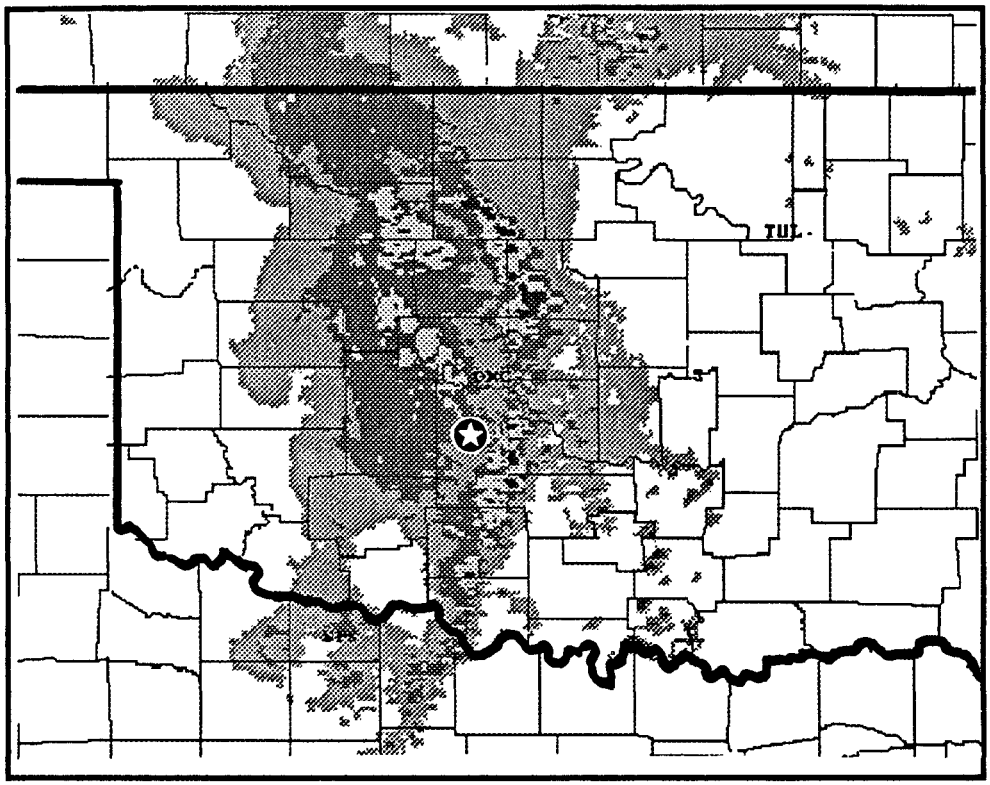

FIG. 4. Location of 0705 UTC 24 May 1991 electric field meter launch site (indicated by star) overlaid on composite of low-level radar reflectivity patterns of the 24 May 1991 (symmetric) MCS at 0700 UTC. Radar reflectivity ranges of 18–30, 30–41, 41–46, and >46 dB*Z*, respectively.

II of this study to initialize hydrometeor advection profiles in the numerical model.

3) ELECTRICAL STRUCTURE

Three electric field profiles were obtained in this system: two near the leading edge of the stratiform precipitation region and one near the trailing edge of the stratiform precipitation region. The two soundings released near the leading edge, by virtue of their in-cloud trajectories, sampled a good deal of the region of mesoscale ascent associated with the region of stratiform precipitation. Here we focus on these two soundings since they were 1) both obtained in a region of deep mesoscale ascent, and 2) exhibited characteristics most similar to the type A profiles presented by Marshall and Rust (1993). The third electric field profile from this system (i.e., the one launched near the trailing edge), though exhibiting many type A characteristics, contained a much larger horizontal electric field component, which was presumably due to its ascent location near the edge of the stratiform precipitation region. Since the presence of large E_h complicates profile interpretation (see the appendix), this sounding will not be discussed here.

Figures 8 and 9 and Tables 1 and 2 depict the two electric field profiles and analyzed charge densities for the 0549 and 0705 EFM flights, respectively. System-relative flight trajectories for these two balloon-borne EFM profiles, though obtained approximately 75 min apart, indicate that they passed through equivalent regions of the MCS stratiform cloud. In a system-relative sense, both EFMs were initially carried toward the convective line in the low-level, rear-to-front flow. Upon ascending above approximately 2 km, however, they were quickly carried rearward over the most intense portion of the radar bright band by the strong, front-to-rear flow. When examining these trajectories with respect to the composited vertical velocity structure (e.g., Figs. 5 and 6), it appears that both EFMs passed through the deepest and most intense portion of the stratiform updraft, which was located near the leading edge of the stratiform precipitation region.

In comparing the two EFM profiles, it is interesting to note the similarities in the vertical charge structures. Both soundings had essentially five layers of charge located near and above the melting level. Furthermore, though launched 75 min apart and at locations separated in distance by more than 50 km (but at approximately the same system-relative location with respect to the convective line), the profiles suggest a steady-state charge structure, at least over this observational period.

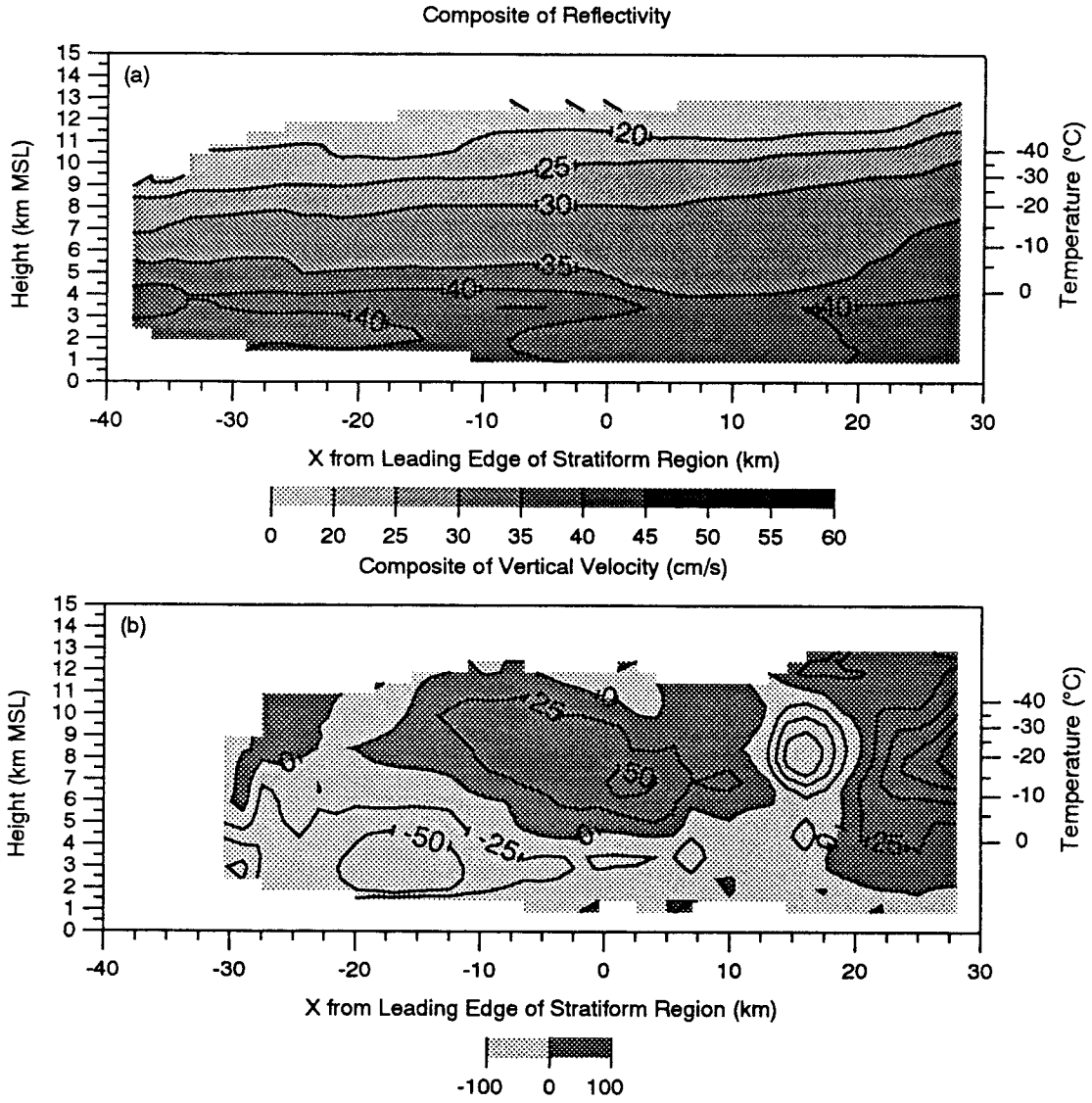

FIG. 5. Composite line-normal profile of (a) radar reflectivity (dBZ), and (b) vertical velocity (cm s^{-1}) constructed from the 0408 UTC 24 May 1991 P-3 flight leg. In (b), dark shading indicates updraft, while light shading indicates downdraft, with vertical velocity contoured every 25 cm s^{-1}. Composite is relative to the leading edge of the stratiform precipitation region.

In both cases, the dominant charge polarity below the melting level, and below cloud base, was negative. A region of positive charge was situated above this region in both soundings. Both EFM soundings also show remarkable similarity in the midlevels, particularly at $T > -12$°C. Maximum stratiform charge densities were approximately 5 nC m^{-3} (see Tables 1 and 2), however, which is as large as those typically observed in convective cores (Marshall and Rust 1993).

b. Asymmetric MCS

At 1200 UTC 7 May 1991, a weak trough extended from a surface low over south-central New Mexico into eastern Colorado. Over the next 12 h, the surface low deepened rapidly and moved eastward toward the Texas Panhandle, resulting in an intensification of south-southeasterly winds over central Oklahoma and west Texas and a subsequent increase in dewpoints to 15°C (an increase by as much as 6°C over 12 h earlier). Warm advection at 850 mb and the approach of a vigorous short-wave trough at 500 mb combined to destabilize the atmosphere over eastern New Mexico and the west Texas Panhandle. As the surface low moved eastward, convection was initiated along the corresponding dryline/trough by 2300 UTC in the central Texas Panhandle. Eventually the convection became organized into a bowed line of convection. As the line moved eastward,

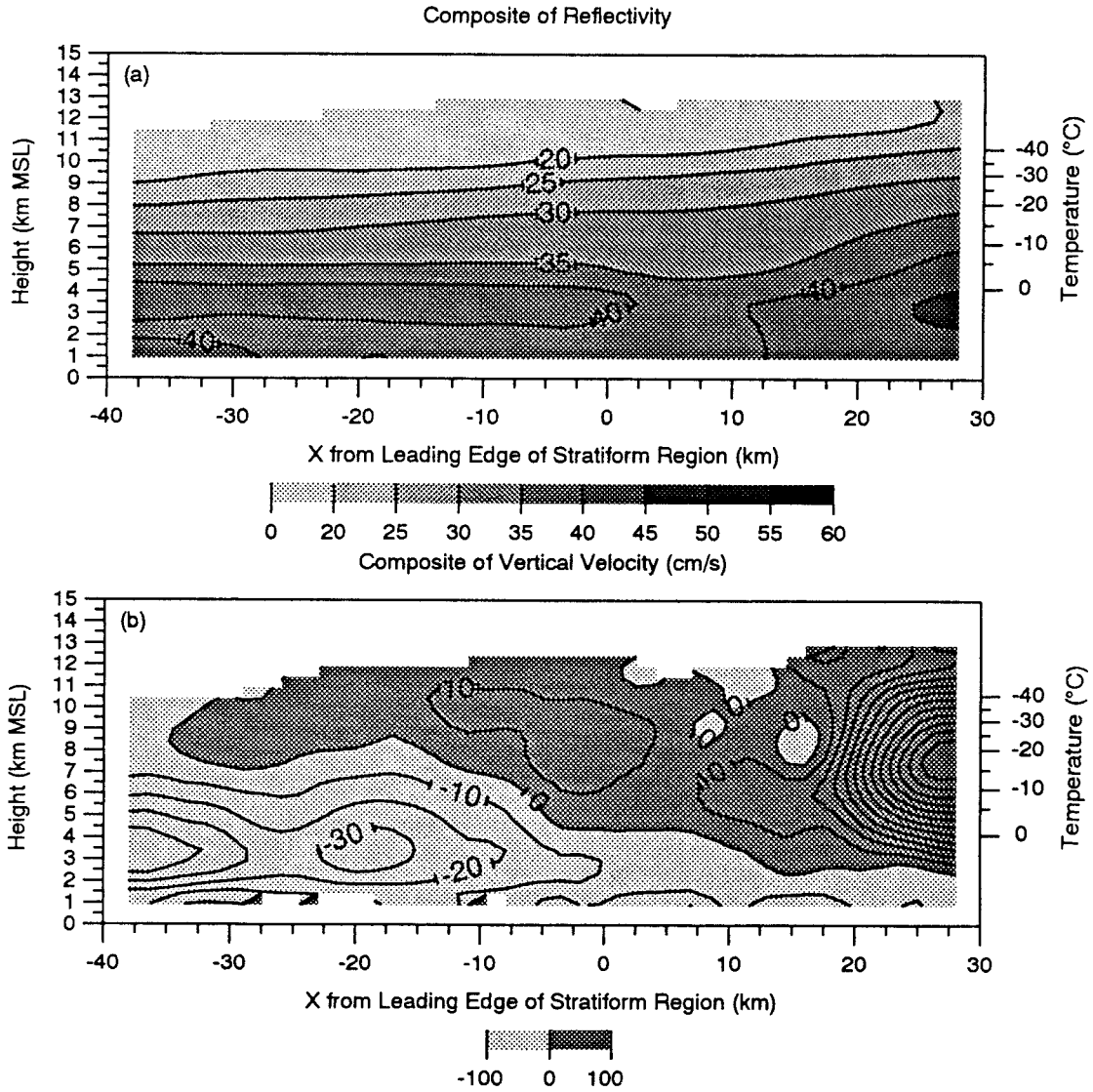

FIG. 6. Composite line-normal profile of (a) radar reflectivity (dBZ), and (b) vertical velocity (cm s^{-1}) constructed from all 24 May 1991 P-3 transition zone/stratiform region flight legs. In (b), dark shading indicates updraft, while light shading indicates downdraft, with vertical velocity contoured every 10 cm s^{-1}. Plotted with respect to the leading edge of the stratiform precipitation region.

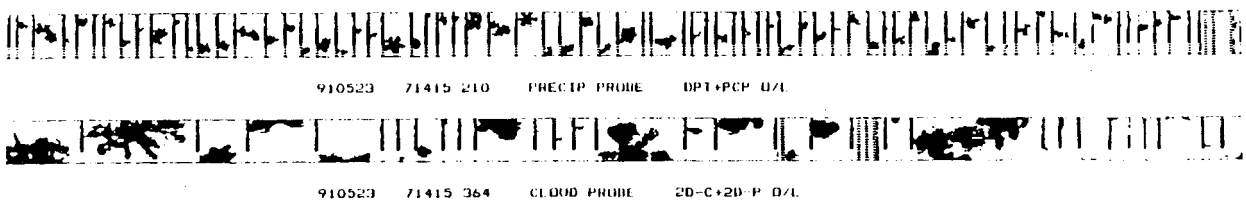

FIG. 7. NOAA P-3 2D shadow graph imagery obtained at a temperature of −8°C in 24 May 1991 MCS.

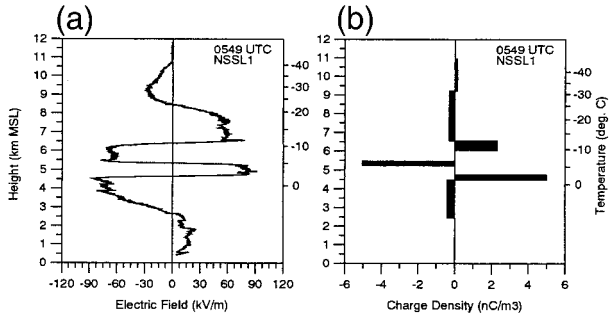

FIG. 8. (a) Electric field profile from the 0549 UTC electric field meter flight. (b) Charge densities (nC m^{-3}) for the 0549 UTC sounding. Location of electric field meter launch is indicated by the star in Fig. 3.

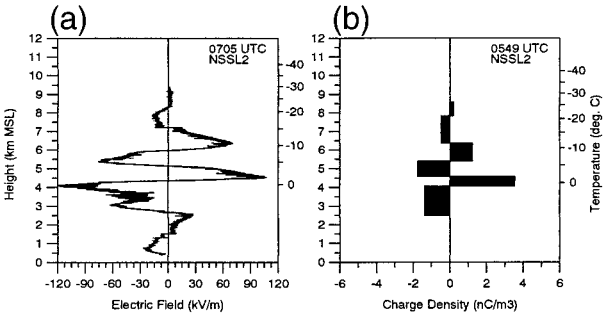

FIG. 9. (a) Electric field profile from the 0705 UTC electric field meter flight. (b) Charge densities (nC m^{-3}) for the 0705 UTC sounding. Location of electric field meter launch is indicated by the star in Fig. 4.

it expanded both to the north and south and eventually formed a line that was nearly north–south oriented in central Oklahoma and east–west oriented in northern Texas (with the apex of the convective line's bow tracking along the Red River). Figures 10 and 11 depict the low-level radar reflectivity structure of the asymmetric MCS at 0700 and 0800 UTC, which are the approximate times (0659 and 0755, respectively) of the two asymmetric MCS EFM flights.

1) KINEMATIC STRUCTURE

As the MCS moved into central Oklahoma, the P-3 conducted two long flight legs (representing ~450 km of aircraft data) through the transition zone. Overall, system-relative winds derived from the dual-Doppler grids exhibited many similarities to those depicted by the asymmetric MCS conceptual model (see Fig. 1b). At low levels, winds were typically weak and from the east. Above this, a gradual veering of the winds resulted in line-parallel (i.e., south-southeasterly) flow at locations immediately behind the convective line. At the line's northern end, winds remained predominantly easterly in apparent response to the mesovortex that was situated over west-central Oklahoma (Jorgensen and Smull 1993). Near the apex in the convective line's bow, winds on the western edge of the analysis grid exhibited a weak westerly component.

Using the two transition zone flight legs, vertical velocities were derived using the compositing technique described in the appendix. Here we present reflectivity and vertical velocity profiles for a space–time composite of both legs (Fig. 12). The 15-km gap in the vertical velocity data in Fig. 12 represents data that were removed from the analysis due to poor quality wind estimates at high radar pointing angles (see the appendix). As revealed by an examination of Fig. 12, the consistency of the vertical velocity observations on either edge of the data gap suggests that the same basic structure was also present in the data void region. Immediately behind the convective line, vertical velocities were positive but relatively weak as remnants of the dissipating convective line were detrained rearward into the trailing stratiform region. In the transition zone, the vertical velocity structure consisted of weak upward motion near cloud top with a deep region of weak descent below. Finally, in the trailing stratiform region, the vertical velocity structure consisted of a deep mesoscale downdraft at $T > -15$°C with weak ascent above that level. It is into this environment that the two asymmetric MCS electric field profiles were obtained.

2) MICROPHYSICAL STRUCTURE

A spiral descent was conducted by the P-3 at the approximate time and location of the first EFM launch. Again the optical array probe (OAP) instrumentation problems resulted in significant data gaps. Nevertheless, as with the symmetric MCS, good quality data were collected at the −8°C level. We therefore present data that focus on observations made at −8°C in order to facilitate a later comparison to data presented earlier at the same temperature level of the symmetric MCS. In the asymmetric MCS, this temperature level was located

TABLE 1. Charge analysis of the 0549 UTC 24 May 1991 (symmetric) MCS electric field profile.

Z_{bot} (km)	Z_{top} (km)	T_{bot} (°C)	T_{top} (°C)	E_{bot} (kV m^{-1})	E_{top} (kV m^{-1})	ρ (nC m^{-3})
2.44	4.47	7.5	−1.3	11.56	−81.64	−0.40
4.47	4.75	−1.3	−1.9	−81.64	72.96	4.99
5.22	5.47	−4.3	−5.8	72.36	−70.34	−5.05
6.04	6.55	−8.8	−11.8	−68.62	63.73	2.30
6.55	9.22	−11.8	−28.5	63.73	−27.13	−0.30
9.22	10.94	−28.5	−43.1	−27.13	−0.80	0.13

TABLE 2. Charge analysis of the 0705 UTC 24 May 1991 (symmetric) MCS electric field profile.

Z_{bot} (km)	Z_{top} (km)	T_{bot} (°C)	T_{top} (°C)	E_{bot} (kV m^{-1})	E_{top} (kV m^{-1})	ρ (nC m^{-3})
2.48	4.06	10.6	0.5	21.49	−104.68	−1.37*
4.06	4.56	0.5	−1.3	−104.68	94.63	3.53
4.56	5.39	−1.3	−6.2	94.63	−69.44	−1.74
5.39	6.36	−6.2	−11.6	−69.44	63.30	1.21
6.36	7.84	−11.6	−21.0	63.30	−15.47	−0.47
7.84	8.57	−21.0	−26.1	−15.47	2.49	0.22

* Representative charge density above and below high horizontal electric field region at approximately 5°C.

approximately in the middle of a deep region of net negative charge.

The shadow graph imagery at −8°C in the asymmetric MCS is presented in Fig. 13. The images indicate that most hydrometeors were small, irregularly shaped ice particles. Some needles were identifiable. Perhaps most striking, however, was the lack of dendritic crystals at −8°C, which suggests the lack of water-saturated conditions at and above that level. This inference is supported by soundings, which indicated slightly subsaturated conditions with respect to water through a deep layer above the −8°C level. Although occasional pockets of LWC $>$ 0.2 g m^{-3} were found on some transition zone flight legs, some showed no cloud water at all or LWCs below the minimum detectable threshold of the instrument (~0.1 g m^{-3}). As with the symmetric MCS, LWCs were averaged over the −8° to −16°C layer of the spiral descent. Although these measurements indicated the occasional presence of at least some cloud water within this layer, they more often indicated a general lack of widespread water-saturated conditions (in support of the conclusions drawn from the shadow imagery).

3) ELECTRICAL STRUCTURE

Two electric field profiles were obtained in the stratiform region of this system. Figures 14 and 15 and Tables 3 and 4 depict the electric field profiles and charge densities (using the procedures described in the

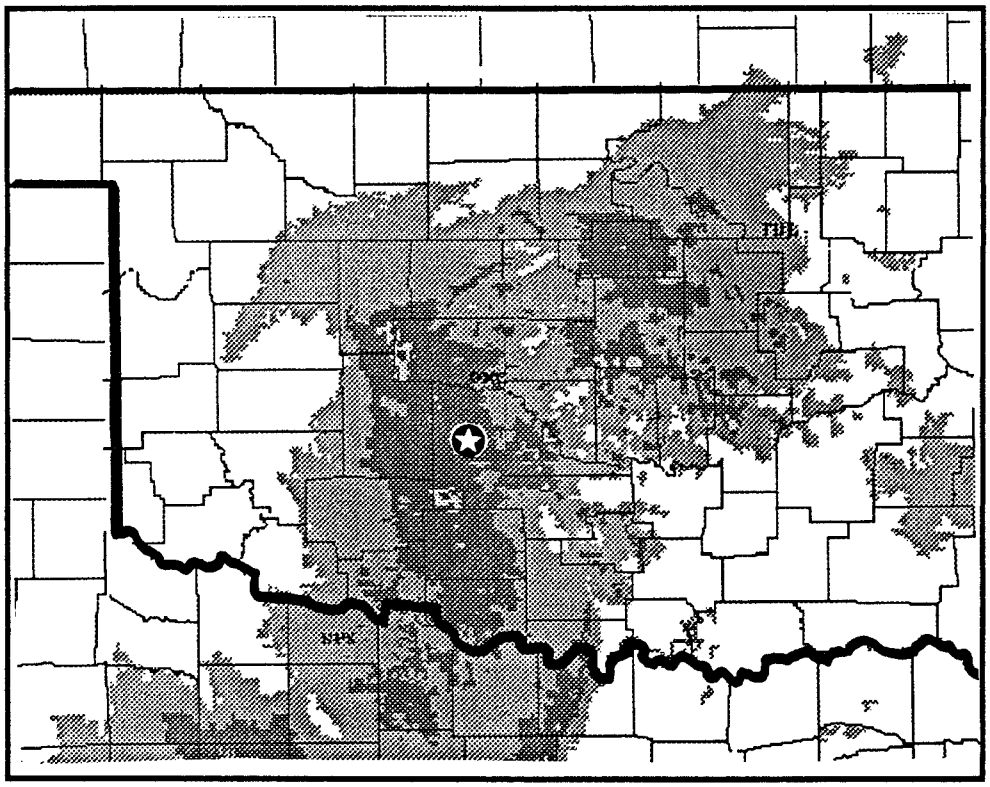

FIG. 10. Location of 0659 UTC 8 May 1991 electric field meter launch site (indicated by star) overlaid on composite of low-level radar reflectivity patterns of the 8 May 1991 (asymmetric) MCS at 0700 UTC. Radar reflectivity ranges of 18–30, 30–41, 41–46, and >46 dBZ, respectively.

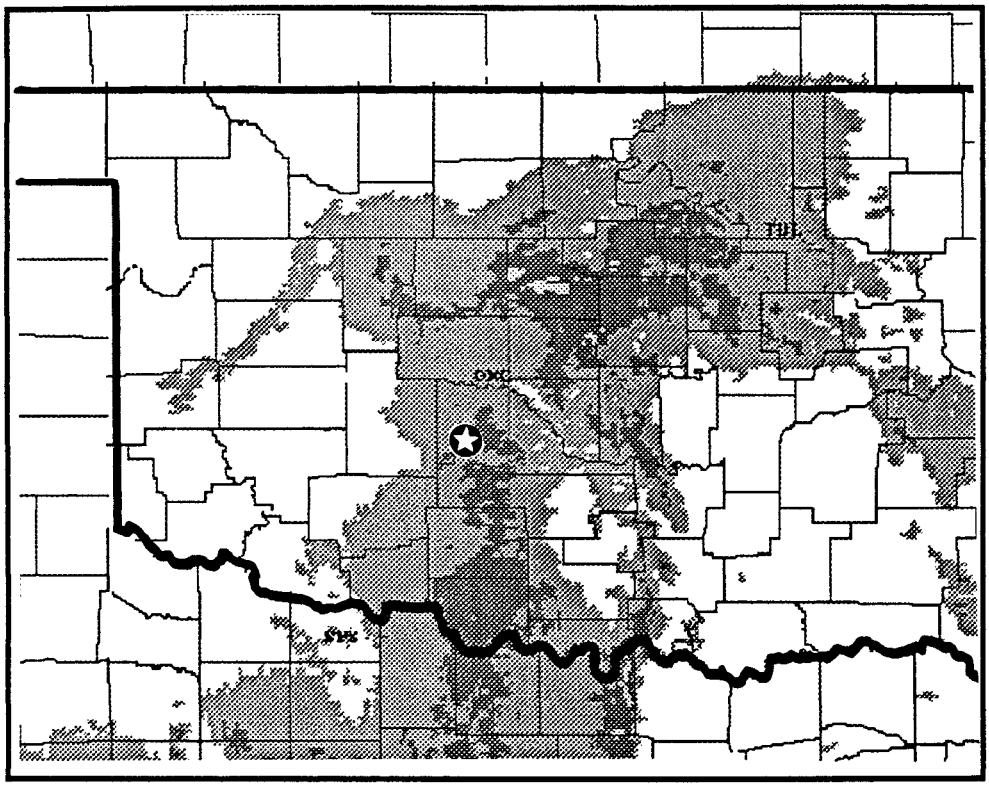

FIG. 11. Location of 0755 UTC 8 May 1991 electric field meter launch site (indicated by star) overlaid on composite of low-level radar reflectivity patterns of the 8 May 1991 (asymmetric) MCS at 0800 UTC. Radar reflectivity ranges of 18–30, 30–41, 41–46, and >46 dBZ, respectively.

appendix) for the 0659 and 0755 EFM flights, respectively. The first EFM was launched at a location toward the leading edge of the stratiform precipitation region. Since there was southeasterly, system-relative flow, the EFM was quickly carried to the northwest as it ascended, eventually passing through the most intense region of the stratiform region bright band. The second EFM was also launched in the stratiform precipitation region, though the intensity and areal coverage of the bright band had decreased dramatically by this time. As noted earlier, both EFM profiles were obtained at a time when the MCS was rapidly dissipating.

The electric field profiles exhibit marked similarities to each other. Furthermore, both soundings had essentially three layers of charge located near and above the melting level. Both electric field profiles exhibited layers of significant positive charge near 0°C that had charge densities between approximately 1.5 and 2.5 nC m^{-3} and electric field magnitudes between 60 and 90 kV m^{-1}. Above this intense lower layer, charge densities were quite weak (<-0.5 nC m^{-3}). Both asymmetric profiles also exhibited rather deep ($\sim$1 km) layers immediately above the lower region of positive charge over which horizontal electric fields were significant and, as a result, charge densities could not be computed. When examining the asymmetric MCS EFM profiles with respect to the kinematic structure presented earlier (Fig. 12), it is apparent that the two EFMs likely ascended through a deep region of mesoscale descent. A less vigorous mesoscale circulation is also supported by the low cloud-top heights at the time of the two EFM launches.

4. Comparison of symmetric and asymmetric MCSs

Previous studies on MCS electrification have proposed two primary charging mechanisms for the trailing stratiform precipitation region: 1) advection of charge from the convective line (Rutledge and MacGorman 1988), and 2) local charge generation resulting from microphysical processes within the stratiform region (Rutledge et al. 1990; Engholm et al. 1990). We now examine and compare the two MCSs' concurrent kinematic, microphysical, and electrical structure from similar perspectives, with these charging mechanisms in mind. A more quantitative investigation of these two electrification mechanisms (for a symmetric MCS) will be presented in Part II.

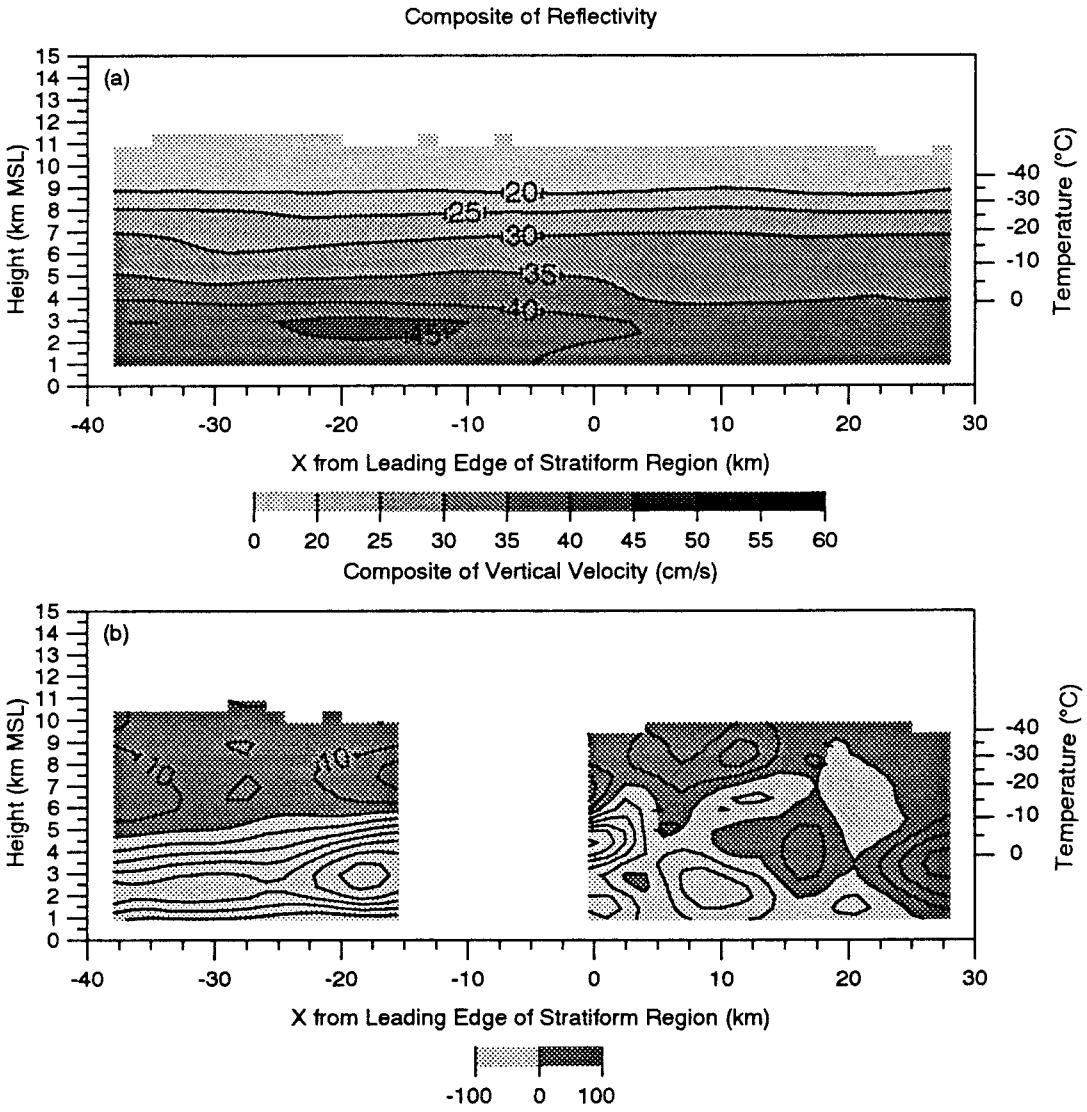

FIG. 12. Composite line-normal profile of (a) radar reflectivity (dBZ,) and (b) vertical velocity (cm s^{-1}) constructed from all 8 May 1991 P-3 transition zone/stratiform region flight legs. In (b), dark shading indicates updraft, while light shading indicates downdraft, with vertical velocity contoured every 10 cm s^{-1}. Composite is relative to the leading edge of the stratiform precipitation region.

a. Summary of kinematic, microphysical, and electrical differences

Before discussing differences that might account for the different electrical structures in these symmetric and asymmetric MCSs, we first present a brief summary of the fundamental kinematic, microphysical, and electrical differences (based on the observations presented in section 3). When comparing the two MCSs kinematic structures, it first should be noted that the symmetric MCS was in its mature stage during P-3 and EFM data collection, while the asymmetric MCS was in its dissipative stage. Furthermore, due to the more southeast-to-northwest orientation of the asymmetric MCS's convective line, the winds in the asymmetric MCS exhibited a much stronger line-parallel component than that in the symmetric MCS. Probably most interesting, however, is a comparison of the two MCSs composite mesoscale vertical velocity structures. The vertical velocity composites indicate that the symmetric MCS (Fig. 6) had a deep mesoscale updraft that was deepest and most intense at a location that preceded the stratiform bright band by about 10 km. The base of the updraft was situated at approximately −5°C. The vertical velocity composite of the asymmetric MCS (Fig. 12), however, indicated that the mesoscale updraft was weak and entirely situated above the −15°C isotherm. Below this level, a mesoscale downward motion was dominant.

In comparing the two MCS microphysical structures,

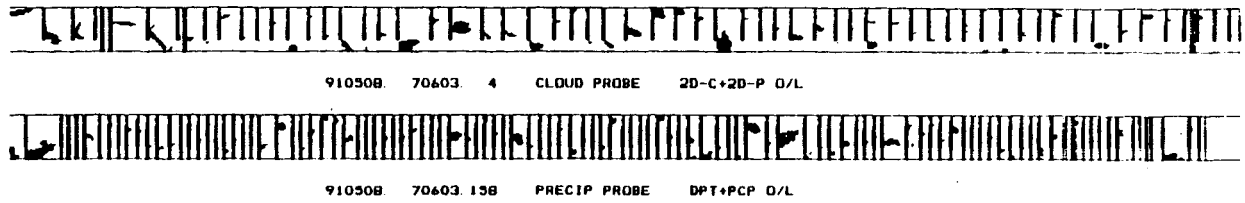

FIG. 13. NOAA P-3 2D shadow graph imagery obtained at a temperature of −8°C in the 8 May 1991 MCS.

we also find several notable differences. Most striking perhaps was the significant dendritic growth in the symmetric MCS and the lack of dendritic growth in the asymmetric MCS. Also, liquid water contents in the asymmetric MCS were noticeably smaller than in the symmetric MCS. Both of these observations suggest that widespread water-saturated conditions were much more prevalent in the symmetric MCS than in the asymmetric MCS, *especially at the levels (between approximately −8° and −16°C) where the more significant differences in the symmetric and asymmetric MCS electric field profiles were observed.* Recall that this temperature level encompassed one of the primary charge transitions in the symmetric MCS electric field profiles. No such charge transition, however, occurred in the asymmetric MCS electric field profiles.

A comparison of the electric field profiles in the symmetric and asymmetric MCSs yields many similarities and differences. In the symmetric MCS, both soundings had essentially five layers of charge located near and above the melting level; in the asymmetric MCS, both soundings had essentially three layers of charge located near and above the melting level. All profiles (symmetric and asymmetric) had an intense layer of positive charge near 0°C. This near-melting level charge transition is a rather common feature in stratiform region EFM soundings. Shepherd et al. (1996) recently examined charge transitions near the melting level of several MCSs and concluded that melting charging [as described by Drake (1968) and Simpson (1909)] is a likely candidate to explain charge layers in this region. It is interesting to note, however, that the positive charge layer in some of these profiles lies entirely above the melting level. This is a feature that was also commonly found in the electric field profiles examined by Shepherd et al. (1996), leading them to speculate on several different mechanisms that might act in unison with particle melting to produce a sharp charge transition at temperatures immediately above the 0°C level. Maximum electric fields and charge densities were larger in the symmetric MCS (100 kV m^{-1} and 5.0 nC m^{-3}) than in the asymmetric MCS (75 kV m^{-1} and 2.5 nC m^{-3}).

b. Advection

In an attempt to understand the microphysical and electrical influences the convective line might have on the trailing stratiform region, dual-Doppler synthesized winds at several analysis times were used to compute trajectories of ice particles detrained from the convective line in each MCS. Hydrometeor fallspeeds were derived by averaging output from a series of extended velocity azimuth display analyses (Srivastava et al. 1986). Trajectories were then computed by tracking the horizontal position of ice particles detrained from the convective line at 8.5 km AGL and advected through dual-Doppler synthesized wind fields. These trajectories were then compared against the mean mesoscale vertical motion structure of each MCS to determine the mean conditions encountered by ice particles as they transected the transition zone and entered the stratiform precipitation region.

The results of this analysis revealed important differences. For the symmetric MCS, all hydrometeors fol-

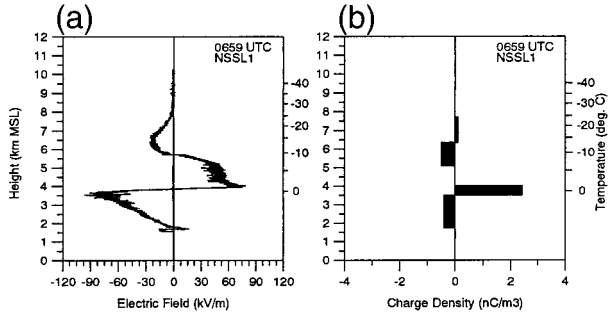

FIG. 14. (a) Electric field profile from the 0659 UTC electric field meter flight. (b) Charge densities (nC m^{-3}) for the 0659 UTC sounding. Location of electric field meter launch is indicated by the star in Fig. 10.

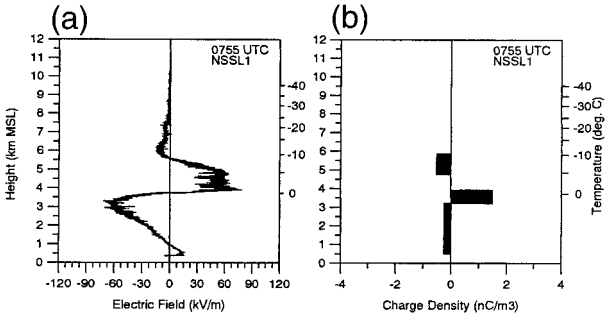

FIG. 15. (a) Electric field profile from the 0755 UTC electric field meter flight. (h) Charge densities (nC m^{-3}) for the 0755 UTC sounding. Location of electric field meter launch is indicated by the star in Fig. 11.

TABLE 3. Charge analysis of the 0659 UTC 8 May 1991 (asymmetric) MCS electric field profile.

Z_{bot} (km)	Z_{top} (km)	T_{bot} (°C)	T_{top} (°C)	E_{bot} (kV m^{-1})	E_{top} (kV m^{-1})	ρ (nC m^{-3})
1.73	3.50	10.6	0.6	4.10	−76.99	−0.41
3.50	4.02	0.6	−1.3	−76.99	66.11	2.43
5.07	6.34	−7.2	−15.2	47.03	−23.03	−0.49
6.34	7.79	−15.2	−25.1	−23.24	−3.03	0.12

lowed rather simple trajectories in which hydrometeors quickly transected the transition zone in the dominant front-to-rear midlevel flow and entered the stratiform region. For the asymmetric MCS, the much stronger line-parallel airflow component resulted in trajectories that more closely followed the convective line. Thus, when compared against the mesoscale vertical velocity structures for the symmetric and asymmetric MCSs (e.g., Figs. 6 and 12, respectively), it is apparent that ice particles detrained from the convective line of the asymmetric system had as much as three times more ''residence time'' in the transition zone downdraft than in the symmetric system. Several studies (e.g., Yeh et al. 1991; Braun and Houze 1994) have indicated that particle growth due to both deposition and aggregation is suppressed in the transition zone downdraft. Given the dependence of most charging theories on the presence of cloud water and/or water-saturated conditions, it is expected that noninductive charging would also be absent or greatly reduced in this region. However, it should be pointed out that the electrical behavior of the thermodynamic zone between ice and water saturation is relatively unexplored due to difficulties in creating these conditions in the laboratory.

c. Stratiform in situ conditions

After passing through the transition zone downdraft, detrained ice particles then entered the stratiform precipitation region and accompanying mesoscale ascent. We begin our analysis of this region by noting that the primary charge structure differences between the symmetric and asymmetric MCS are between approximately 0° and −12°C, where the symmetric MCS exhibited two distinct charge layers that were not present in the asymmetric soundings. Figure 16 depicts the two symmetric MCS electric field profiles with respect to the 0°, −12°, and −40°C temperature levels. These three temperature levels are the same as depicted in the microphysical conceptual model presented in section 1; thus, Fig. 16 can be compared against Fig. 2 to understand the mean microphysical conditions associated with each charge transition level in the symmetric MCS.

Houze (1989) noted that the 0° to −12°C layer is significant since ice particles readily aggregate within this temperature zone. Additionally, Houze noted that riming may also take place within this region. Though in situ observations of MCS stratiform supercooled liquid water contents are quite limited, our observations indicate that mixed-phase conditions were present to at least −20°C (the maximum altitude attained by the P-3 aircraft) in the symmetric MCS; observations in the asymmetric MCS indicated significantly less supercooled cloud water. These key microphysical differences are consistent with the substantial differences in the depth and magnitude of the mesoscale updraft between these two cases (cf. Figs. 5b and 12b). Evidently the stronger mesoscale updraft in the symmetric case supported the presence of supercooled cloud water and obviously water-saturated conditions.

Figure 17 depicts the mean charge layers, which are derived from a combination of electric field profiles obtained in each MCS, overlaid on a conceptual model depicting depositional growth regimes (from Hallett 1984). The positive charge layer located immediately below −12°C in our symmetric MCS electric field profiles is also located immediately below the level at which ice growth by the Bergeron–Findeisen process (e.g., Bergeron 1935; Findeisen 1938) achieves a maximum (approximately −15°C at a pressure of 65 kPa). In addition, as can be seen from Fig. 17, dendritic growth is favored at temperatures colder than −12°C in water-saturated conditions. Microphysical observations in the symmetric MCS indicated the presence of dendritic growth, which is consistent with water-saturated conditions. In contrast, ice particles observed in the same temperature zone in the asymmetric MCS indicated no dendritic features. Combined, these observations indicate that, at a minimum, cloud water was clearly not as abundant or widespread in the asymmetric MCS as in the symmetric MCS. Both symmetric MCS electric field profiles also had charge transitions (though of opposite polarity) immediately above the melting level. Figure 17 depicts the negative above positive charge transition that was found immediately above the melting level in

TABLE 4. Charge analysis of the 0755 UTC 8 May 1991 (asymmetric) MCS electric field profile.

Z_{bot} (km)	Z_{top} (km)	T_{bot} (°C)	T_{top} (°C)	E_{bot} (kV m^{-1})	E_{top} (kV m^{-1})	ρ (nC m^{-3})
0.50	3.21	12.0	2.3	12.72	−60.63	−0.24
3.21	3.93	2.3	−1.2	−60.63	60.75	1.49
4.75	5.87	−6.0	−12.3	55.27	−10.00	−0.52

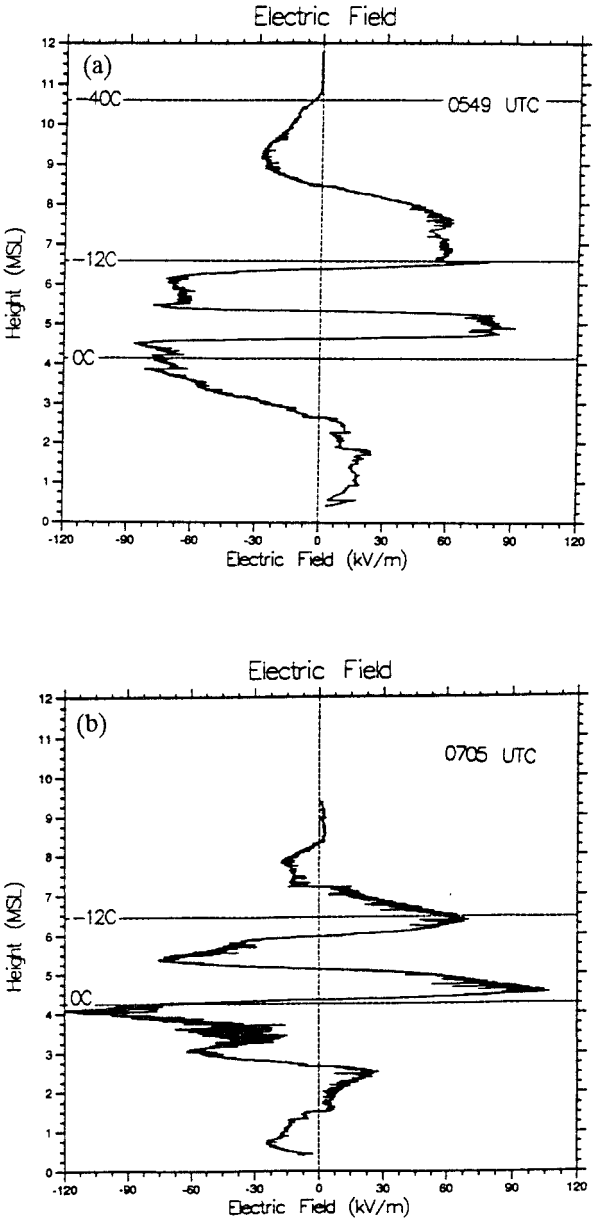

FIG. 16. Symmetric MCS electric field profiles at (a) 0549 and (b) 0705 UTC with 0°, −12°, and −40°C temperature levels overlaid.

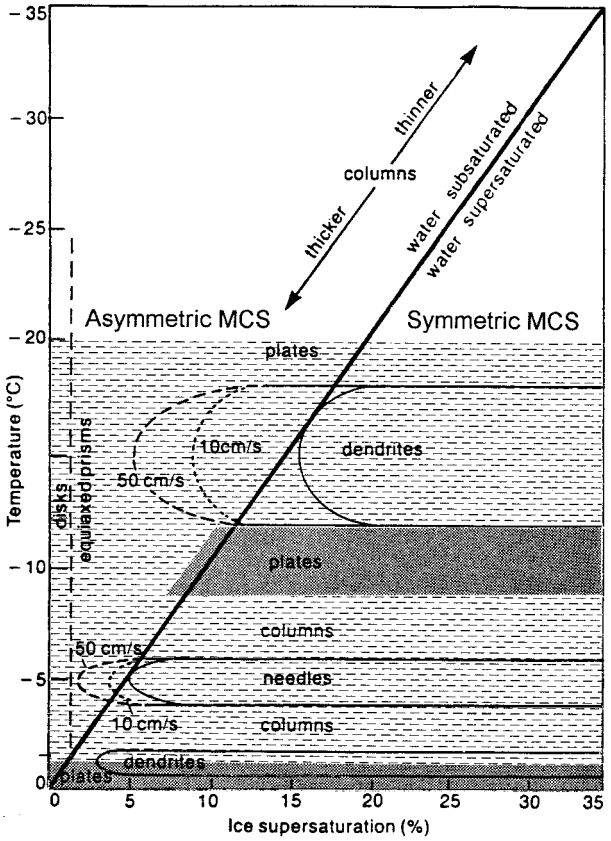

FIG. 17. Composite charge layers from symmetric and asymmetric MCS overlaid on figure depicting depositional growth regimes. The solid diagonal line running from the lower left corner to the upper right corner represents boundary between water subsaturated conditions (on the left) and water-saturated conditions (on the right). Positive charge layers are indicated by dark shading and negative charge layers by light shading. Charge profile to right of diagonal line (see text) is representative of symmetric MCS while charge profile to left of diagonal line (see text) is representative of asymmetric MCS. (Adapted from Hallett 1984.)

one of the symmetric electric field profiles and both of the asymmetric electric field profiles.

The importance of these levels are further examined by analyzing the charge structure in the symmetric case in the context of mean and maximum aggregate sizes. For this analysis, we overlay our derived symmetric MCS charge structure on data for stratiform clouds by Hobbs et al. (1974; see Fig. 18). By comparing the peaks in maximum aggregate size to the levels at which charge transitions occurred in the symmetric electric field profiles, it is apparent that both the upper and lower charge transitions are collocated with peaks in expected maximum aggregate size. It should be noted that lower charge transitions in *both* the symmetric and asymmetric MCS electric field profiles were found at temperatures of approximately −1.3°C (i.e., above the melting level). These levels are also collocated with a peak in maximum aggregate size. In a study of the stratiform region of another MCS, Willis and Heymsfield (1989) found that the region immediately above the melting level, in addition to having large aggregates, was also a region where large concentrations of small ice crystals were commonly found.

These observations suggest that particle separation due to fallspeed differences is a possible candidate to explain the charge transitions immediately above the melting level and also near the −12°C isotherm. That is, if a charging mechanism [e.g., the noninductive mechanism; Takahashi (1978)] allowed large and small ice particles to obtain opposite polarity charge, then subsequent aggregation coupled with fallspeed differ-

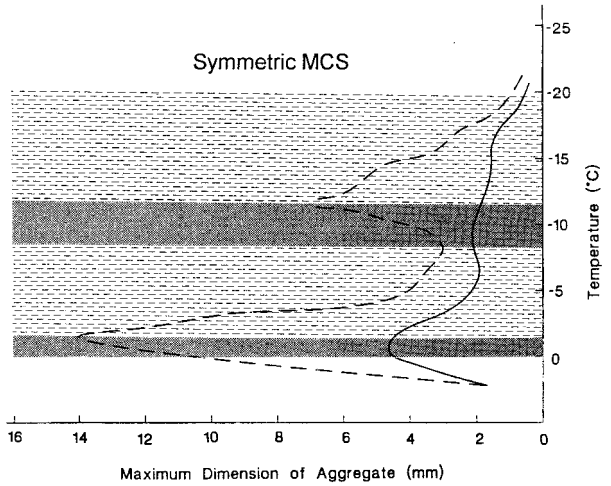

FIG. 18. Composite charge layers from symmetric MCS overlaid on profiles of mean and maximum aggregate sizes. The solid curve represents the mean aggregate size, and the dashed line represents the maximum aggregate size (data from Hobbs et al. 1974). Positive charge layers are depicted by dark shading, negative charge layers by light shading. (Adapted from Hobbs et al. 1974 and Young 1993.)

ences between particle types may be sufficient to explain a charge transition that coincides with these peak aggregation layers (aggregates separating from smaller crystals by virtue of their slightly larger fallspeeds). In the asymmetric MCS, both kinematic and microphysical observations suggest that dendritic growth at temperatures near $-12°C$ was not supported. Also, an aggregation peak was not observed in this region, in contrast to the symmetric case.

5. Discussion and conclusions

We examined the concurrent kinematic, microphysical, and electrical structures of two mesoscale convective systems. The results of these comparisons are summarized by the conceptual models in Figs. 19 and 20. The orientation of the cross sections depicted in Figs. 19 and 20 is along a line analogous to AB in the symmetric and asymmetric conceptual models (cf. Figs. 1a,b), respectively.

The mesoscale vertical motion structure of the symmetric MCS consisted of a deep transition zone downdraft, which was apparently at least partially forced in the upper levels by convergence of convective outflows (Fig. 19). Trailing this transition zone downdraft was a region of deep mesoscale ascent. Mesoscale ascent was deepest and most intense near the leading edge of the radar bright band. Matejka and Schuur (1991) found a similar vertical motion structure in another symmetric MCS and proposed that this location represented a region of enhanced depositional growth. In our case, both EFMs (launched near the leading edge of the stratiform bright band) were quickly caught up in the strong midlevel, front-to-rear flow and carried rearward into this region of mesoscale ascent. As the EFMs ascended into the mesoscale updraft, they encountered a deep layer of water-saturated conditions that favored dendritic growth. By comparison, the mesoscale vertical motion structure of the asymmetric MCS consisted of deep descent in the transition zone region (Fig. 20). The vertical velocity structure of the stratiform precipitation region was characterized by mesoscale descent below approximately $-15°C$ and mesoscale ascent above. At the time of the EFM data collection in the asymmetric MCS, the convective line had dissipated significantly and the transition zone was much wider than that observed in the symmetric MCS.

Marshall and Rust (1993) suggested that the different electrical structures of these two MCSs might be related to differences in MCS flow structure, microphysical processes, or both. Our observations revealed several notable differences between symmetric and asymmetric MCSs. First, particle trajectories computed from three-dimensional wind fields suggest that ice particles advected from the convective line of the asymmetric MCS followed a much more line-parallel path (with smaller line-normal velocities) than did ice particles advected from the convective line of the symmetric MCS. As a result, an ice particle's ''residence time'' in the transition zone downdraft was as much as three times longer in the asymmetric MCS than in the symmetric MCS. Several studies (e.g., Yeh et al. 1991; Braun and Houze 1994) have indicated that mass growth due to both deposition and aggregation is suppressed in the transition zone downdraft. Given the dependence of several microphysical charging theories on the presence of cloud water, it is anticipated that noninductive charging would be absent or greatly reduced in the transition zone. Second, upon reaching the MCS stratiform precipitation region, advected ice particles in each system encountered quite different kinematic and thermodynamic environments. Composited data from the NOAA P-3 tail-Doppler radar indicate that the symmetric MCSs mesoscale updraft was deepest and most intense near the leading edge of the stratiform precipitation region (the approximate location where the two primary electric field profiles ware obtained). Furthermore, measurements of supercooled liquid water contents exceeding 0.2 g m^{-3} and observations of dendritic growth both support the presence of widespread water-saturated conditions. By comparison, the asymmetric MCSs composited vertical velocity structure exhibited a deep layer of descent, which would have suppressed supercooled liquid water. In situ aircraft observations indicate that water-saturated conditions were much less widespread and dendritic growth much less prevalent in the asymmetric MCS, consistent with extensive downward motion in the MCS stratiform region. We believe these contrasting kinematic and microphysical structures are at least partially responsible for the differences in the observed electrical structures. In particular, enhanced depositional growth afforded by water-saturated con-

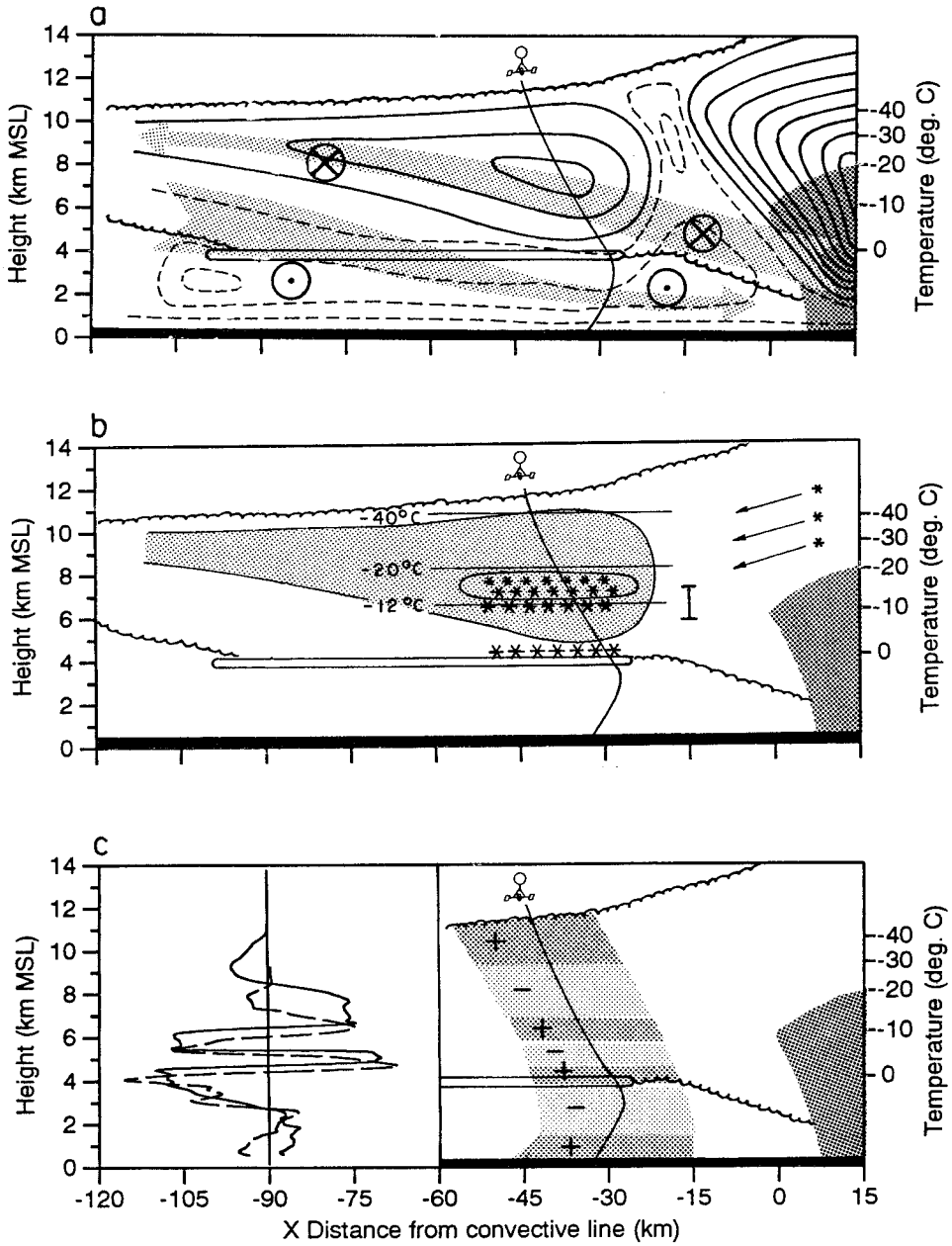

FIG. 19. Conceptual model depicting (a) kinematic, (b) microphysical, and (c) electrical structure of symmetric MCS. In (a), light shading indicates line-normal, system-relative airflow, while line-parallel, system-relative airflow into and out of the of the cross section are indicated by (⊗) and (○), respectively. Solid (dashed) contours represent location and relative strength of updraft (downdraft). In (b), light shading indicates location of mesoscale updraft from (a). Locations of the aggregation regions (cf. Fig. 18) are represented by (*), while the (I) symbol indicates the −8° to −16°C layer over which P-3 LWCs were averaged. In (c), dark shading represents positive charge layers and light shading negative charge layers (composited from the 0549 and 0705 UTC 24 May 1991 electric field profiles on the left). The system-relative trajectories of the three EFM flights on 24 May 1991 are shown in (a), (b), and (c). The 0549 and 0705 UTC trajectories, which were launched in similar system-relative locations, are overlaid and form the right trajectory.

ditions, followed by gravitational separation of large and small ice particles, is argued to have produced the additional two charge layers found near −12°C in the symmetric MCS case.

As noted by the conceptual models, the multiple balloon-borne electric field observations into each MCS revealed very different electrical structures. EFM ascents in the symmetric MCS indicated five layers of

charge (at $T \leq 0°C$), while profiles in the asymmetric MCS had a much simpler vertical structure consisting of three layers of charge (at $T \leq 0°C$). Peak electric fields were >100 kV m^{-1} in the symmetric MCS and >80 kV $^{-1}$ in the asymmetric MCS. The multiple profiles further suggest that stratiform electrical structures exhibited very little spatial and temporal variability at least over the course of the EFM observations, which spanned several hours.

In both MCS stratiform regions, the sharpest charge transition (positive charge above negative or negative charge above positive) and largest charge density magnitudes were typically situated immediately above the 0°C isotherm (typically within 350 m of the 0°C isotherm). Furthermore, the symmetric MCS also had a sharp charge transition (negative charge above positive) near the −12°C isotherm. Because of the close proximity between the lowest charge transition and the melting level, past studies (i.e., Shepherd et al. 1996) have invoked melting-driven charging mechanisms (Drake 1968; Simpson 1909) to explain the charge transition near the melting level. When we compare these charge levels in detail to the results from Hobbs et al. (1974), we find that both occur at temperatures where aggregation efficiency is high and large aggregates are commonly found (see Fig. 18). Therefore, we suggest that if opposite polarities of charge already exist on large and small hydrometeors as a result of noninductive (e.g., Takahashi 1978), fragmentation (e.g., Avila and Caranti 1994), or some other charging process, it is possible that subsequent fallspeed differences between aggregates and smaller ice particles could then result in a sharp charge transition near both the melting and −12°C levels. Charge transitions near these two levels were also noted by Schuur et al. (1991) and Hunter et al. (1992) for other MCSs.

While the observational analysis indicates that the symmetric and asymmetric MCSs had very different concomitant kinematic, microphysical, and electrical structures, it should be noted that the data obtained in each system were collected at different stages of their life cycles. That is, the majority of the data in the symmetric MCS were collected during the mature stage, while the majority of the data in the asymmetric MCS were collected during the dissipative stage. Since several studies have indicated that symmetric-type MCSs often evolve into asymmetric MCSs later in their lifetime, it is possible that a similar evolution from a type A to a type B electrical structure (e.g., Marshall and Rust 1993) might occur. That is, as a system evolves from a symmetric to asymmetric structure, the concurrent dynamical evolution of the MCS stratiform precipitation region, as influenced by heat and hydrometeor advection from the convective line, might also result in an evolution of the electrical structure.

While this observational study provides insight into possible kinematic and microphysical influences on MCS charge distribution, the data are insufficient to address the relative contribution of possible charging mechanisms. In particular, both charge advection from the convective line and charge generation from local microphysical processes have been proposed as significant contributors. In Part II we will examine both of these mechanisms in more detail with numerical simulations.

Acknowledgments. We would like to thank Dr. Thomas Marshall of the University of Mississippi and Dr. W. David Rust of the National Severe Storms Laboratory for providing us with the electric field meter data. Though too numerous to mention, the many participants in the 1991 Cooperative Oklahoma Profiler Studies project are acknowledged for their time spent collecting the multiple datasets used in this study. In particular, David Johnson of the National Severe Storms Laboratory assisted in the editing and early analysis of the airborne Doppler data. Drs. W. David Rust and Conrad Ziegler reviewed earlier versions of this manuscript. The comments of Dr. Earle Williams and two anonymous reviewers are also greatly appreciated. Finally, we thank Drs. Walt Petersen and Larry Carey for their valuable input during the course of this research. This research was supported by NOAA/National Severe Storms Laboratory through Contract NA900RAH00077 and the National Science Foundation through Grants ATM-9015485, ATM-9321361, and ATM-9726464.

APPENDIX

Data Collection and Analysis Methods

a. Radar data

During the EFM flights, a NOAA P-3 research aircraft (N43RF) executed flight legs that documented the MCSs kinematic and microphysical structures. The primary source of radar data used in this study was provided by the P-3's vertically scanning, X-band (3.2 cm) tail-Doppler radar (e.g., Jorgensen et al. 1983; Parrish 1989). During COPS91, radar data were collected using the fore–aft scanning technique (FAST, e.g., Frush et al. 1986; Hildebrand 1989; Jorgensen and Smull 1993; Jorgensen et al. 1996] whereby two scans of data are collected in sequence: one pointing approximately 25° forward, and the other approximately 25° aft of a plane normal to the aircraft track. Thus, as the aircraft executes a quasi-linear flight leg, a three-dimensional region of intersecting beams is created. When the antenna is rotated at its maximum rotation rate of 10 rpm (60° s^{-1}) at a typical aircraft speed of 120 m s^{-1}, the FAST scanning results in intersecting, adjacent beams at a horizontal resolution of approximately 1.5 km.

Prior to the construction of dual-Doppler wind fields from these intersecting beams, an aircraft motion of approximately 50 m s^{-1} (introduced into the data by the ~120 m s^{-1} ground speed and ~25° antenna pointing angle) was removed from the radial velocity data. Ve-

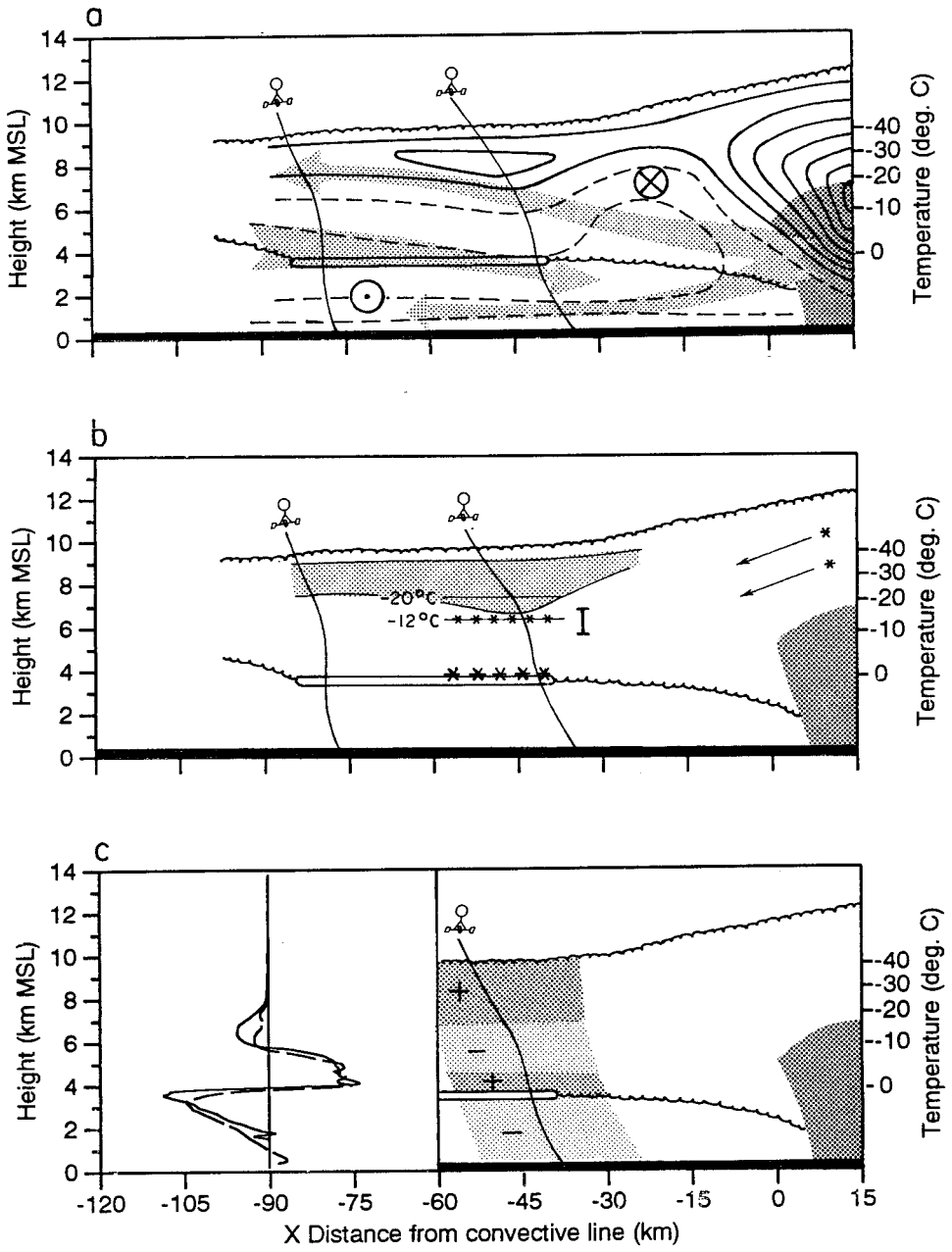

FIG. 20. Same as Fig. 19, except for asymmetric MCS. The system-relative trajectories of the two EFM flights on 8 May 1991 (0659 and 0755 UTC) are shown in (a), (b), and (c).

locity artifacts resulting from improper antenna alignment were also removed. According to Jorgensen (1984), this process results in radial velocity estimates that are accurate to within 1.5 m s^{-1}. The data were then unfolded to remove velocity aliasing and objectively transferred to grids with a data spacing of 1.5 km in the horizontal and 0.5 km in the vertical. Storm motions of 11.7 m s^{-1} from 270° and 11.2 m s^{-1} from 285° were computed and removed from the dual-Doppler winds of the symmetric and asymmetric MCSs, respectively. A Shuman (1957) filter was then applied to the U and V winds, which, assuming an error variance of 1.5 m s^{-1}, resulted in a subsequent vertical velocity resolution of approximately 1 m s^{-1}. Integration of the divergence profiles using the anelastic form of the equation of mass continuity was then performed to obtain vertical motion fields. Downward integrations were adjusted according to O'Brien (1970) in order to ensure zero vertical velocities at both ground and cloud top.

Because of the many inherent errors in airborne Doppler radar observations (e.g., Hildebrand 1989; Jorgensen et al. 1996) and furthermore, uncertainties in

determining the upper boundary condition (e.g., Shuman 1957; Biggerstaff and Houze 1991; Jorgensen et al. 1996), it is often impossible to resolve mesoscale vertical motions to within 10–50 cm s^{-1} (typical of mesoscale motions). Therefore, many studies (e.g., Smull and Houze 1987; Matejka and Schuur 1991; Biggerstaff and Houze 1993) rely upon either spatial and/or temporal averages of dual-Doppler grids to resolve mesoscale vertical motions. In this study, we average vertical velocity data from 10 available dual-Doppler grids for the symmetric (24 May 1991) MCS case and two available dual-Doppler grids for the asymmetric (8 May 1991) MCS to create line-normal, system-relative composites of radar reflectivity, horizontal winds, and mesoscale vertical motion (oriented along a line in each system analogous to AB in Fig. 1) over which microphysical and electrical analyses may be overlaid. In the process of creating the composited profiles, several steps were taken to ensure data quality. Foremost, since the P-3's tail-Doppler radar is a vertically scanning radar, poor estimates of the horizontal winds are often made at high pointing angles, thereby resulting in a cone of data both above and below the aircraft where horizontal wind estimates are unreliable. This problem is frequently compounded at high pointing angles by contributions from falling hydrometeors. By examining dual-Doppler analyses at several times, it was determined that the contribution from these two effects was unacceptable at locations within 15 km of the aircraft track. Since subsequent flight legs were flown at a variety of distances behind the convective line (ranging from 10 to 40 km), however, this data gap does not appear in our space–time composite.

Thus, the resulting composite represents an average over both space and time and is therefore most similar to the averaging technique used by Biggerstaff and Houze (1993). Since convective lines are not always completely linear nor necessarily aligned with the dual-Doppler grid (as is often the case in our study), a strict N–S linear average has the possibility of introducing significant errors by ''aliasing'' higher vertical motions from more rearward positioned convective cells into the mesoscale vertical motion profile. Therefore, we composite the data with respect to two system-relative frames of reference: 1) the leading edge of the trailing stratiform precipitation region and 2) the leading edge of the transition zone. This procedure allows us to unambiguously address the vertical velocity structure of the transition zone and trailing stratiform precipitation region, thus minimizing aliasing of convective vertical motions resulting from any nonlinearity of the convective line. All dual-Doppler composites constructed in this manner were then averaged over time to develop the final, 3-h space–time composite. We focus on composites constructed with respect to the leading edge of the stratiform precipitation region.

b. Microphysical data

The P-3 collected in situ cloud microphysical data within each MCS, including two-dimensional particle image data for both cloud and precipitation particle sizes using the 2D-C (50–1600 μm) and 2D-P (200–6400 μm) optical array probes (OAPs; Knollenberg 1970, 1976). Additionally, cloud liquid water contents were measured by a Johnson–Williams (JW) liquid water content meter. The OAPs provide two-dimensional images of ice particles (hereafter referred to as shadow graph imagery) from which information on the composition and growth mode of the ice particles may be inferred. The JW liquid water content probe uses a heated platinum wire to sense cloud water drops that are primarily less than 30–40 μm in diameter (Knollenberg 1972).

Though the majority of the P-3 flight in each MCS was spent on constant altitude passes in the transition zone, advecting spiral descents (e.g., Lo and Passarelli 1982) were also conducted in each system at the approximate time and location of EFM flights (presented later). In the advecting spiral descent, the aircraft spirals downward in a constant bank angle at the approximate fallspeed of the hydrometeors. Data from the advecting spiral descent in each system were qualitatively analyzed and compared at similar levels to ascertain any microphysical differences that might account for the MCS's different electrical structures. An analysis comparing the OAP data of the advecting spiral descents in these two systems has also been completed by Hendricks (1993). Additionally, we compare cloud liquid water contents by averaging the JW data by temperature level for each flight and comparing the results to the radar-derived mesoscale vertical motion structure and OAP shadow graph imagery.

In this study, computer software similar to that described by Jorgensen and Willis (1982) is used to process the 2D-C and 2D-P OAP data. Unfortunately, due to intermittent OAP vibration problems that resulted in the occasional misalignment of diodes, microphysical data were often of insufficient quality to produce time series of hydrometeor concentrations over complete flight legs. The data did, however, allow us to determine hydrometeor concentrations on an occasional basis. These concentrations, most of which were collected in the MCS transition zone region, are used in Part II of this study to initialize microphysical profiles immediately behind the convective line for the numerical simulations.

c. Electric field meter data

Vertical profiles of electric field measured by balloon-borne EFMS were a central component of this study. The EFMs used in COPS91 (Fig. A1) are described in detail by numerous previous studies (e.g., Winn et al. 1978; Schuur et al. 1991; Stolzenburg et al. 1994; Shepherd et al. 1996; Stolzenburg 1996). During COPS91,

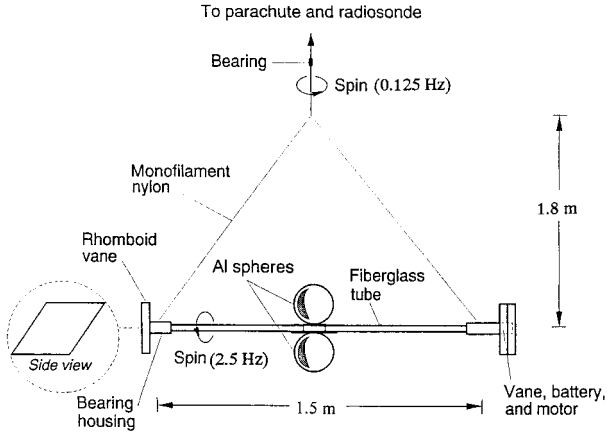

FIG. A1. Electric field meter used during COPS91. Equal and opposite charges induced upon the spheres by rotation about the horizontal axes allow for the computation of vertical and horizontal components of the electric field vector, respectively.

two NSSL mobile laboratories (hereafter referred to as NSSL1 and NSSL2, Rust 1989) were deployed to locations in advance of developing MCSs. EFMs were then launched into the MCSs as they passed over the launch sites. The EFMs were flown on a 1200-g helium-filled balloon, at the end of an instrument chain that included a parachute, Vaisala RS80 radiosonde, and, occasionally, a particle/charge measuring instrument (e.g., Bateman et al. 1994). In postprocessing, the thermodynamic and electric field datasets were interpolated and combined to provide vertical profiles of the electric field (e.g., Schuur et al. 1991).

In this analysis, as in previous studies, E denotes the magnitude of the total electric field vector $\mathbf{E}$, E_z the magnitude of the vertical component of $\mathbf{E}$, and E_h the magnitude of the horizontal component of $\mathbf{E}$. Here E_z is taken to be positive when an upward directed force is exerted on a positive test charge. Therefore, in the fair weather atmosphere where the earth has a negative charge, E_z is negative (i.e., $\mathbf{E}_z$ is directed downward) and has a value of approximately -100 V m^{-1}. As described earlier, the EFM is capable of measuring both E_z and E_h. However, the electric field profiles typically find that E_h magnitudes are small compared to E_z magnitudes.

Using the EFM measurements, the charge density ρ may be computed using Gauss' law, which states that ρ is proportional to the divergence of the electric field vector, that is,

$$\nabla \cdot \mathbf{E} = \frac{\rho}{\varepsilon_o}, \tag{A1}$$

where ε_o (8.86×10^{-12} F m^{-1}) is the permittivity of air. Since this study focuses on electric field measurements in MCS stratiform clouds, which typically exhibit stratified thermodynamic and microphysical environments, and furthermore since E_h ($<$30 kV m^{-1}) was small compared to E_z ($>$90 kV m^{-1}), we assume that the charge is distributed in horizontally extensive layers. We further confine the analysis to appreciably deep regions where $\partial E_z/\partial z$ is nearly constant and the charge density in Eq. (A1) is approximated as

$$\rho \approx \varepsilon_o\left(\frac{\Delta E_z}{\Delta z}\right). \tag{A2}$$

Therefore, when the balloon is ascending, the slope of the electric field profile has the same sign as the polarity of charge found within that layer and the magnitude of the slope is proportional to the magnitude of the charge density. Whereas many previous studies (e.g., Schuur et al. 1991; Hunter et al. 1992) have used this analysis method to examine charge regions in detail, the analysis presented in this study follows the more restrictive criteria set forth by Stolzenburg et al. (1994) in that changes in E_z that result in charge layers where either 1) $|\rho| < 0.1$ nC m^{-3}, 2) $\Delta z < 200$ m, or 3) $|\rho \Delta z| < 50$ nC m^{-2} are ignored. A more detailed discussion of the procedures used in the EFM analysis may be found in Schuur et al. (1991), Stolzenburg et al. (1994), and Shepherd et al. (1996).

REFERENCES

Avila, E. E., and G. M. Caranti, 1994: A laboratory study of static charging by fracture in ice growing by riming. *J. Geophys. Res.*, **99,** 10 611–10 620.

Bateman, M. G., W. D. Rust, and T. C. Marshall, 1994: A balloon-borne instrument for measuring the charge and size of precipitation particles inside thunderstorms. *J. Atmos. Oceanic Technol.*, **11,** 161–169.

Bergeron, T., 1935: On the physics of clouds and precipitation. *Proc. Fifth Assembly Int. Union Geodesy Geophys.*, Lisbon, Portugal, 156–178.

Biggerstaff, M. I., and R. A. Houze Jr., 1991: Kinematic and precipitation structure of the 10–11 June 1985 squall line. *Mon. Wea. Rev.*, **119,** 3034–3065.

——, and ——, 1993: Kinematics and microphysics of the transition zone of the 10–11 June 1985 squall line. *J. Atmos. Sci.*, **50,** 3091–3110.

Blanchard, D. O., 1990: Mesoscale convective patterns of the southern high plains. *Bull. Amer. Meteor. Soc.*, **71,** 994–1005.

Braun, S. A., and R. A. Houze Jr., 1994: The transition zone and secondary maximum of radar reflectivity behind a midlatitude squall line: Results retrieved from Doppler radar data. *J. Atmos. Sci.*, **51,** 2733–2755.

Drake, J. C., 1968: Electrification accompanying the melting of ice particles. *Quart. J. Roy. Meteor. Soc.*, **94,** 176–191.

Engholm, C. D., E. R. Williams, and R. M. Dole, 1990: Meteorological and electrical conditions associated with positive cloud-to-ground lightning. *Mon. Wea. Rev.*, **118,** 470–487.

Findeisen, W., 1938: Die Kolloidmeteorologischen Vorgange der Niedershlagsbildung. *Meteor. Z.*, **55,** 121–133.

Fovell, R. G., and Y. Ogura, 1988: Numerical simulation of a midlatitude squall line in two dimensions. *J. Atmos. Sci.*, **45,** 3846–3879.

Frush, C. L., P. H. Hildebrand, and C. Walther, 1986: The NCAR airborne Doppler radar. Part II: System design considerations. Preprints, *23d Conf. on Radar Meteorology*, Snowmass, CO, Amer. Meteor. Soc., 151–154.

Hallett, J., 1984: How snow crystals grow. *Amer. Sci.*, **72,** 582–589.

Hendricks, W. Z., 1993: Hydrometeor spectra and cloud electrifica-

tion. Ph.D. dissertation, University of Nevada, 212 pp. [Available from Dept. of Physics, University of Nevada, Reno, NV 89506.]

Hildebrand, P. H., 1989; Airborne Doppler radar accuracy. Preprints, *24th Conf. on Radar Meteorology*, Tallahassee, FL, Amer. Meteor. Soc., 585–588.

Hobbs, P. V., S. Chang, and J. D. Locatelli, 1974: The dimensions and aggregation of ice crystals in natural cloud. *J. Geophys. Res.*, **79,** 2199–2206.

Houze, R. A., Jr., 1989: Observed structure of mesoscale convective systems and implications for large-scale heating. *Quart. J. Roy. Meteor. Soc.*, **115,** 425–461.

——, and D. D. Churchill, 1984: Microphysical structure of winter monsoon cloud clusters. *J. Atmos. Sci.*, **41,** 3405–3411.

——, S. A. Rutledge, M. I. Biggerstaff, and B. F. Smull, 1989: Interpretation of Doppler weather radar displays of midlatitude mesoscale convective systems. *Bull. Amer. Meteor. Soc.*, **70,** 608–619.

——, B. F. Smull, and P. Dodge, 1990: Mesoscale organization of springtime rainstorms in Oklahoma. *Mon. Wea. Rev.*, **118,** 613–654.

Hunter, S. M., T. J. Schuur, T. C. Marshall, and W. D. Rust, 1992: Electrical and kinematic structure of the Oklahoma mesoscale convective system of 7 June 1989. *Mon. Wea. Rev.*, **120,** 2226–2239.

Jorgensen, D. P., 1984: Mesoscale and convective-scale characteristics of mature hurricanes. Part I: General observations by research aircraft. *J. Atmos. Sci.*, **41,** 1268–1285.

——, and P. T. Willis, 1982: A *Z–R* relationship for hurricanes. *J. Appl. Meteor.*, **21,** 356–366.

——, and B. F. Smull, 1993: Mesovortex circulations seen by airborne Doppler radar within a bow-echo mesoscale convective system. *Bull Amer. Meteor. Soc.*, **74,** 2146–2157.

——, P. H. Hildebrand, and C. L. Frush, 1983: Feasibility test of an airborne pulse-Doppler meteorological radar. *J. Climate Appl. Meteor.*, **22,** 744–757.

——, T. Matejka, and J. D. DuGranrut, 1996: Multi-beam techniques for deriving wind fields from airborne radars. *J. Meteor. Atmos. Phys.*, **59,** 83–104.

Keller, V., and J. Hallett, 1982: Influence of air velocity on the habit of ice crystal growth from the vapor. *J. Cryst. Growth*, **60,** 91–106.

Knollenberg, R. G., 1970: The optical array: An alternative to scattering or extinction for airborne particle size determination. *J. Appl. Meteor.*, **9,** 86–103.

——, 1972: Comparative liquid water content measurements of conventional instruments with an optical array spectrometer. *J. Appl. Meteor.*, **11,** 501–508.

——, 1976: Three new instruments for cloud physics measurements: The 2-D spectrometer, the forward scattering spectrometer probe, and the active scattering aerosol spectrometer. *Proc. Int. Conf. on Cloud Physics*, Boulder, CO, Amer. Meteor. Soc., 554–561.

Leary, C. A., and R. A. Houze Jr., 1979: Melting and evaporation of hydrometeors in precipitation from anvil clouds of deep tropical convection. *J. Atmos. Sci.*, **36,** 669–679.

Lo, K. K., and R. E. Passarelli Jr., 1982: The growth of snow in winter storms: An airborne observational study. *J. Atmos. Sci.*, **39,** 697–706.

Loehrer, S. M., and R. H. Johnson, 1995: Surface pressure and precipitation life cycle characteristics of PRE-STORM mesoscale convective systems. *Mon. Wea. Rev.*, **123,** 600–621.

MacGorman, D. R., and W. D. Rust, 1998: *The Electrical Nature of Storms*. Oxford University Press, 422 pp.

Magono, C., and C. W. Lee, 1966: Meteorological classification of natural snow crystals. *J. Fac. Sci. Hokkaido Univ. Ser. VII*, **2,** 321.

Marshall, T. C., and W. D. Rust, 1993: Two types of vertical electrical structures in stratiform precipitation regions of mesoscale convective systems. *Bull. Amer. Meteor. Soc.*, **74,** 2159–2170.

Matejka, T., and T. J. Schuur, 1991: The relationship between vertical air motions and the precipitation band in the stratiform region of a squall line. Preprints, *25th Int. Conf. on Radar Meteorology*, Paris, France, Amer. Meteor. Soc., 501–504.

O'Brien, J. J., 1970: Alternative solutions to the classical vertical velocity problem. *J. Appl. Meteor.*, **9,** 197–203.

Orville, R. E., R. W. Henderson, and L. F. Bosart, 1988: Bipole patterns revealed in lightning locations in mesoscale storm systems. *Geophys. Res. Lett.*, **15,** 129–132.

Parish, J. R., 1989: New NOAA WP-3D Doppler radar system. Preprints, *24th Conf. on Radar Meteorology*, Tallahassee, FL, Amer. Meteor. Soc., 615–618.

Rasmussen, E. N., and S. A. Rutledge, 1993: Squall line evolution. Part I: Kinematics and reflectivity structure. *J. Atmos. Sci.*, **50,** 2584–2606.

Rotunno, R., J. B. Klemp, and M. L. Weisman, 1988: A theory for strong, long-lived squall lines. *J. Atmos. Sci.*, **45,** 463–485.

Rust, W. D., 1989: Utilization of a mobile laboratory for storm electricity measurements. *J. Geophys. Res.*, **94,** 13 305–13 311.

Rutledge, S. A., and R. A. Houze Jr., 1987: A diagnostic modeling study of the trailing stratiform region of a midlatitude squall line. *J. Atmos. Sci.*, **44,** 2640–2656.

——, and D. R. MacGorman, 1988: Cloud-to-ground lightning activity in the 10–11 June 1985 mesoscale convective system observed during OK PRE-STORM. *Mon. Wea. Rev.*, **116,** 1393–1408.

——, and W. A. Petersen, 1994: Vertical radar reflectivity structure and cloud-to-ground lightning in the stratiform region of MCSs: Further evidence for in-situ charging in the stratiform region. *Mon. Wea. Rev.*, **122,** 1760–1776.

——, R. A. Houze Jr., M. I. Biggerstaff, and T. J. Matejka, 1988: The Oklahoma–Kansas mesoscale convective system of 10–11 June 1985: Precipitation structure and single-Doppler radar analysis. *Mon. Wea. Rev.*, **116,** 1409–1430.

——, C. Lu, and D. R. MacGorman, 1990: Positive cloud-to-ground lightning in mesoscale convective systems. *J. Atmos. Sci.*, **47,** 2085–2100.

Ryan, B. F., E. R. Wishart, and D. E. Shaw, 1976: The growth rates and densities of ice crystals between −3°C and −21° C. *J. Atmos. Sci.*, **33,** 842–850.

Schuur, T. J., 1997: An observational and modeling study of Mesoscale Convective System electrification. Dept. of Atmospheric Science, Paper 628, Colorado State University, Fort Collins, CO, 302 pp. [Available from Dept. of Atmospheric Science, Colorado State University, Fort Collins, CO 80523.]

——, and S. A. Rutledge, 2000: Electrification of Stratiform regions in Mesoscale Convective Systems. Part II: Two-dimensional numerical model simulations of a symmetric MCS. *J. Atmos. Sci.*, **57,** 1983–2006.

——, B. F. Smull, W. D. Rust, and T. C. Marshall, 1991: Electrical and kinematic structure of the stratiform precipitation region trailing an Oklahoma squall line. *J. Atmos. Sci.*, **48,** 825–841.

Shepherd, T. R., W. D. Rust, and T. C. Marshall, 1996: Electric fields and charges near 0°C in stratiform clouds. *Mon. Wea. Rev.*, **124,** 919–938.

Shuman, F. G., 1957: Numerical methods in weather prediction: II. Smoothing and filtering. *Mon. Wea. Rev.*, **85,** 357–361.

Simpson, G. C., 1909: On the electricity of rain and its origin in thunderstorms. *Philos. Trans. Roy. Soc. London*, **A209,** 379–413.

Smull, B. F., and R. A. Houze Jr., 1985: A midlatitude squall line with a trailing region of stratiform rain: Radar and satellite observations. *Mon. Wea. Rev.*, **113,** 117–133.

——, and ——, 1987: Dual-Doppler radar analysis of a midlatitude squall line with a trailing region of stratiform rain. *J. Atmos. Sci.*, **44,** 2128–2148.

Srivastava, R. C., T. J. Matejka, and T. J. Lorello, 1986: Doppler radar study of the trailing anvil region associated with a squall line. *J. Atmos. Sci.*, **43,** 356–377.

Stolzenburg, M., 1996: An observational study of electrical structure in convective regions of mesoscale convective systems. Ph.D.

dissertation, University of Oklahoma, 137 pp. [Available from School of Meteorology, University of Oklahoma, Norman, OK 73019.]

——, T. C. Marshall, W. D. Rust, and B. F. Smull, 1994: Horizontal distribution of electrical and meteorological conditions across the stratiform region of a mesoscale convective system. *Mon. Wea. Rev.,* **122,** 1777–1797.

Takahashi, T., 1978: Riming electrification as a charge generation mechanism in thunderstorms. *J. Atmos. Sci.,* **35,** 1536–1548.

Willis, P. T., and A. J. Heymsfield, 1989: Structure of the melting layer in mesoscale convective system stratiform precipitation. *J. Atmos. Sci.,* **46,** 2008–2025.

Winn, W. P., C. B. Moore, C. R. Holmes, and L. G. Byerley III, 1978: Thunderstorm on July 16, 1975, over Langmuir Laboratory: A case study. *J. Geophys. Res.,* **83,** 3079–3092.

Yeh, J., F. Beifan, W. R. Cotton, and M. A. Fortune, 1991: Observational study of microphysics in the stratiform region and transition region of a mid-latitude mesoscale convective complex. *Acta Meteor. Sin.,* **5,** 527–540.

Young, K. C., 1993: *Microphysical Processes in Clouds.* Oxford University Press, 427 pp.

Zrnić, D. S., N. Balakrishnan, C. L. Ziegler, V. N. Bringi, K. Aydin, and T. Matejka, 1993: Polarimetric signatures in the stratiform region of a mesoscle convective system. *J. Appl. Meteor.,* **32,** 678–693.